



AMERICAN METEOROLOGICAL SOCIETY

Journal of the Atmospheric Sciences

EARLY ONLINE RELEASE

This is a preliminary PDF of the author-produced manuscript that has been peer-reviewed and accepted for publication. Since it is being posted so soon after acceptance, it has not yet been copyedited, formatted, or processed by AMS Publications. This preliminary version of the manuscript may be downloaded, distributed, and cited, but please be aware that there will be visual differences and possibly some content differences between this version and the final published version.

The DOI for this manuscript is doi: 10.1175/JAS-D-18-0046.1

The final published version of this manuscript will replace the preliminary version at the above DOI once it is available.

If you would like to cite this EOR in a separate work, please use the following full citation:

Khain, P., R. Heiblum, U. Blahak, Y. Levi, H. Muskatel, E. Vadislavsky, O. Altaratz, I. Koren, G. Dagan, J. Shpund, and A. Khain, 2018: Parameterization of vertical profiles of governing microphysical parameters of shallow cumulus cloud ensembles using LES with bin microphysics. *J. Atmos. Sci.* doi:10.1175/JAS-D-18-0046.1, in press.



**Parameterization of vertical profiles of governing microphysical parameters of shallow
cumulus cloud ensembles using LES with bin microphysics**

Pavel Khain¹, Reuven Heiblum², Ulrich Blahak³, Yoav Levi¹, H. B. Muskatel¹, Elyakom
Vadislavsky¹, Orit Altaratz², Ilan Koren², Guy Dagan², Jacob Shpund⁴ and Alexander Khain⁴

¹The Israel Meteorological Service, Israel

²Weizmann Institute of Science, Israel

³Deutscher Wetterdienst, Germany

⁴Hebrew University of Jerusalem, Israel

Submitted to Journal of the Atmospheric Sciences

February 2018

Revision July 2018

Second revision November 2018

Communicating author: Pavel Khain, e-mail: pavelkh_il@yahoo.com

Abstract

Shallow convection is a sub-grid process in cloud-resolving models for which their grid-box is larger than the size of small cumulus clouds (Cu). At the same time such Cu substantially affect radiation properties and thermodynamic parameters of the low atmosphere. The main microphysical parameters used for calculation of radiative properties of Cu in cloud resolving models are liquid water content (LWC), effective droplet radius and cloud fraction (CF). In this study, these parameters of fields of small warm Cu are calculated using large-eddy-simulations (LES) performed using the System for Atmospheric Modelling (SAM) with spectral bin microphysics. Despite the complexity of microphysical processes several fundamental properties of Cu were found: a) Despite the high variability of LWC and droplet concentration within clouds and between different clouds, the volume mean and effective radii per specific level vary only slightly; b) the values of effective radius are close to those forming during adiabatic ascent of air parcels from cloud base.

These findings allow characterizing a cloud field by a specific vertical profiles of effective radius and of mean liquid water content, which can be calculated using the theoretical profile of adiabatic liquid water content and the droplet concentration at cloud base. Using the results of these LES, a simple parameterization of cloud-field averaged vertical profiles of effective radius and of liquid water content is proposed for different aerosol and thermodynamic conditions. These profiles can be used for calculation of radiation properties of Cu fields in large scale models. The role of adiabatic processes in the formation of microstructure of Cu is discussed.

Key words: small Cu, large-eddy simulations, cloud microphysics, parameterization

1. Introduction. Microphysical parameters determining the radiative properties of cloud ensembles

Small warm cumulus clouds (Cu) in the boundary layer (BL) play an important role in the atmospheric radiation and moisture budgets (Trenberth, 2011; Stephens et al., 2012). These clouds are frequent over both the oceans and continents (Norris, 1998) and are responsible for the largest uncertainty in tropical cloud feedbacks in climate models (Bony and Dufresne, 2005). Hence, an accurate calculation of radiative properties of such clouds is of crucial importance for weather prediction, simulation of global circulation and climate, including climatic changes.

The dynamical and microphysical properties of small maritime Cu were measured in-situ in several field experiments: The Small Cumulus Microphysics Study (SCMS) (Gerber, 2000), the Barbados Oceanographic and Meteorological Experiment (BOMEX) (Holland et al. 1973; Siebesma, 2003); the Rain In Cumulus over the Ocean (RICO) (Gerber et al., 2008; Arabas et al., 2009); The Cloud, Aerosol, Radiation and Turbulence In the Trade Wind Regime over Barbados (CARRIBA) (Katzwinkel et al., 2014; Schmeissner et al., 2015).

Small Cu over the land were investigated in Gulf of Mexico Atmospheric Composition and Climate Study (GoMACCS) (Jiang et al., 2008; Lu et al., 2008) and the Routine Atmospheric Radiation Measurement Aerial Facility Clouds with Low Optical Water Depths Optical Radiative Observations (RACORO) field campaign (Lu et al., 2014).

Comparison of cloud properties in clean air over ocean and in polluted air over the land allows investigating effects of aerosols on dynamics, geometrical structure of cloud fields and on cloud microphysics. Aerosols act as cloud condensation nuclei (CCN), on which droplets can form. Polluted clouds have initially smaller and more numerous droplets (Squires, 1958; Squires and Twomey, 1960; Warner and Twomey, 1967; Twomey, 1977). Cloud microphysical and dynamical

processes are coupled, making the cloud system complex. Changes in the initial droplet size distribution (DSD) (driven by changes in the aerosol number concentration) affect processes like condensation efficiency (Pinsky et al., 2013; Seiki and Nakajima 2014; Dagan et al., 2015), latent heat fluxes and vertical velocities (Pinsky and Khain, 2002, Pinsky et al, 2013, 2014; Koren et al. 2014; Dagan et al, 2015), the ability of the droplets to move with the ambient air (Koren et al. 2015), collision-coalescence (Shaw, 2003; Benmoshe et al, 2012), sedimentation and rain production (see reviews Rosenfeld et al., 2008, Khain 2009, Levin and Cotton, 2009; Tao et al, 2012; Khain et al., 2015). In the early stages of the cloud development in polluted air, more and smaller droplets provide more surface area for condensation than in clouds developing in clean air. At these stages, the enhanced condensation yields more latent heat release and enhancement of the updrafts. Moreover, the smaller droplets have better mobility and, therefore, will be pushed higher in the atmosphere by the updrafts, all of which form the theoretical basis for warm clouds invigoration (Koren et al. 2014). Convective invigoration was observed in warm clouds (Kaufman et al., 2005; Yuan et al., 2011; Koren et al. 2005, 2014). At the same time, faster evaporation increases turbulence on the cloud edge and, therefore, the entrainment of dry ambient air into the cloud, which reduces the cloud fraction (CF) (Xue and Feingold 2006; Small et al., 2009; Dagan et al., 2017).

The radiative properties of warm clouds depend on their extent and optical properties. Therefore, changes in the aerosol properties imply changes in the clouds radiative effects. The reflectance of polluted clouds is likely to increase (Twomey 1974, 1977). Moreover, delay in the onset of drizzle implies changes in the shallow clouds liquid water path, optical depth, lifetime and coverage (Albrecht, 1989; Jiang et al., 2006; Small et al., 2009). When considering aerosol induced feedbacks in the cloud field scale the picture becomes even more complicated as the aerosol

properties affect the way by which clouds change the environmental thermodynamics (Khain 2009; Heiblum et al, 2016 a,b; Dagan et al., 2016).

Large scale models in which small warm clouds are subgrid phenomena require a parameterization of small Cu properties including the microphysical and dynamical response of the Cu fields to changes in aerosol properties in the BL.

This study shows that despite the high complexity of microphysical processes, vertical profiles of many basic quantities may be parameterized using results of LES.

There are three basic parameters that are used in large scale models for characterizing radiation and microphysical properties of small clouds: CF, LWC and effective radius, r_e , which is the ratio between the third and second moments of the (DSD) (e.g., Twomey, 1977; Nakajima and King, 1990; Rosenfeld and Lensky, 1998; Blahak and Ritter, 2013). Effective radius together with LWC allow evaluating the integral cross-section of droplets in clouds, which is needed for radiation calculations. Observational studies of cloud tops of growing non-precipitating clouds (Gerber, 2000; Gerber et al, 2008; Freud et al., 2008, 2011; Rosenfeld et al. 2008; Prabha et al., 2011; Katzwinkel et al, 2014; Schmeissner et al. 2015) show a low variability of r_e along horizontal levels. The existence of “a robust vertical profile” of $r_e(z)$ for certain environmental (thermodynamic and aerosol) conditions follows also from observations that the first radar echo appears for different clouds within a cloud field nearly at the same height (Andreae et al, 2004; Freud and Rosenfeld, 2012). The same conclusion was reached from numerical simulations with bin microphysics cloud models (Benmoshe et al., 2012; Khain et al., 2013). It may indicate of the existence of a mean vertical profile of $r_e(z)$ in a cloud field that can represent well non-precipitating clouds of different sizes and lifetime stages.

111 In polluted clouds, the effective radius grows with height slower than in clean clouds. This
112 aerosol dependence allowed Rosenfeld et al. (2014) to use r_e measured from satellites near cloud
113 tops for evaluating the aerosol concentration below cloud base.

114 If the concept of “a robust vertical profile” of r_e for certain environmental (thermodynamic
115 and aerosol) conditions is valid, it can substantially simplify the problem of parameterization of
116 radiative fluxes from fields of cumulus clouds of different sizes and at different stages of their
117 evolution.

118 Formation of raindrops makes the problem of determination of robust $r_e(z)$ profile more
119 complicated because precipitation affects vertical profile of effective radius and decreases droplet
120 concentration and cloud water content (CWC). Note, however, that optical properties of Cu cloud
121 field are determined largely by small cloud droplets, and not by raindrops (Wiscombe et al., 1984;
122 Savijarvi et al., 1997; Savijarvi and Raisanen, 1998).

123 In Section 2 we describe the theoretical background concerning calculation of basic
124 microphysical parameters in cloud resolving numerical weather prediction (NWP) models and the
125 role of large-eddy simulations (LES) utilization. Model setup is presented in Section 3. The LES
126 results are given in Section 4. In Section 5 we suggest a new parameterization of microphysical
127 parameters of cloud ensembles. Section 6 is dedicated to comparison of results of calculations with
128 in-situ observations, as well as to analysis of sensitivity of results (and parameterization) to
129 thermodynamic conditions and model grid spacing. The paper ends with discussion and
130 conclusions.

132 2. Theoretical background

133 2.1 Calculation of shallow cumulus LWC and r_e in NWP models

Large-scale models with grid spacing of tens of kilometers do not resolve clouds and, hence, they use convective parameterization schemes. The values of effective radius and LWC are prescribed in such models, which inevitably leads to errors in calculation of related quantities. The treatment of clouds in meso-scale *cloud-resolving models* (CRM) with grid spacing of a few kilometers is quite complicated because only the largest (grid scale) clouds are resolved in such models. Small clouds and especially shallow warm cumulus clouds (Cu), with a typical size smaller or similar to the grid spacing of CRM remain sub-grid phenomena.

In CRM calculations of effective drop radii at resolvable scales are performed when the relative humidity (RH) in the grid point exceeds 100%. When the grid spacing is larger than the size of shallow Cu, the conditions for small clouds formation can be suitable even when the calculated mean grid relative humidity (RH) is lower than 100%. These clouds may, however, affect the radiative budget substantially, and the knowledge of r_e , LWC and CF values is necessary for such calculations.

In the limited area NWP r_e of unresolved clouds is a tuning parameter. For instance, in the model COSMO (Doms and Schattler, 2002; Steppeler et al., 2003) (for details see webpage: <http://cosmo-model.org>) $r_e = 5 \mu m$ by default. Since on average over the grid box there is subsaturation, the LWC in these shallow cumuli is crudely parameterized as a function of temperature (reduces with a decrease in temperature), mimicking the reduction of available water vapor for condensation with height. Recently, a new cloud radiation scheme was developed for COSMO (Blahak and Ritter, 2013), and is currently under evaluation. Among other developments, r_e of unresolved clouds is calculated in this scheme from the ratio of LWC and droplet concentration. While LWC is evaluated using the parametrization described above, the droplet concentration is determined using the assumed aerosol concentration and the effective

(unresolved) vertical velocity at cloud base (see Section 4.3). The large uncertainty in LWC causes r_e to be highly uncertain as well. As a result, such parameterizations may lead to significant errors in evaluation of effects of shallow convection on radiation and on other thermodynamic atmospheric properties.

2.2 Utilization of LES for simulation of small Cu and parameterization goals

An efficient method to simulate fields of small Cu and investigate Cu dynamics and microphysics, or to develop new parameterizations is LES. In LES clouds are simulated explicitly using a high model resolution that varies from 250 m (Abel and Shipway, 2007) to, in rare cases, 10-25 m (Matheou et al., 2011; Dawe and Austin, 2012; Seifert et al, 2015). Typical grid spacing used for simulation of small Cu is 100 m (Siebesma et al, 2003; Jiang et al., 2008; Heiblum et al, 2016 a,b; Dagan et al., 2016). Taking into account sharp changes of microphysical values in the vertical direction, the vertical grid spacing is usually smaller (typically 40 m) than in the horizontal.

To simulate cloud microphysical processes in such models two main microphysical methods are used: bulk parameterization and bin microphysics (see a review by Khain et al. 2015). The bulk schemes solve microphysical equations for a few moments of the DSD, assuming a specific DSD shape.

LES using bulk-parameterizations microphysical schemes typically focus on investigating effects of thermodynamical and microphysical parameters on the Cu fields, cloud fraction, surface fluxes and mass fluxes and precipitation (e.g., Siebesma et al, 2003; Abel and Shipway 2007). Seifert and Heus (2013) and Seifert et al. (2015) used the University of California, Los Angeles large-eddy simulation (UCLA-LES) model (Stevens et al. 1999) with two-moment bulk-parameterization scheme to investigate the spatial organization of precipitating trade wind cumulus

clouds and the evolution of cloud size distributions under different aerosol concentration conditions. They stressed substantial effect of environment air humidity on the structure of simulated cloud fields.

In bulk schemes the characteristic radius of drops in particular grid points is calculated using the predicted values of LWC and predicted or diagnosed droplet concentration (N_d). The serious difficulties arising in such calculations using one, two- and three-moments bulk parameterization schemes are discussed by Milbrandt and Yau (2005), and Milbrandt and McTaggart-Cowan (2010).

The more detailed microphysical approach is the bin microphysics, which solves the microphysical equations for determining the droplet size distributions (DSD). This method is expensive computationally which hinders its applicability in large scale CRM.

In LES simulations the bin-microphysical approach is often used for investigation of thermodynamic factors and aerosols on the parameters of droplet size distributions, drizzle formation and on cloud dynamics (e.g., Jiang et al., 2008). Such parameters as LWC, droplet concentration and effective radius are determined directly from the calculated DSD.

Small cumulus cloud fields were simulated by Zhang et al. (2011) and Heiblum et al. (2016a,b) using the System for Atmospheric Modelling (SAM) (Khairoutdinov and Randall, 2003). Zhang et al. (2011) analyzed the simulated vertical profiles of effective radius (using the SAM with microphysical method of moments, Tsvion et al. 1987; Reisin et al. 1996) and confirmed the validity of the hypothesis made by Rosenfeld and Lensky (1998) concerning the possibility to retrieve $r_e(z)$ using the values of effective radius measured remotely (from satellites) in tops of developing Cu. Using the SAM with spectral bin microphysics (SBM) described by

Khain et al. (2004, 2013), Heiblum et al. (2016a,b) found substantial dependence of center of gravity of cloud mass on aerosol concentrations.

In addition to bin –microphysics LES models, a new type of models, sometimes referred to as Lagrangian Cloud Models (LCM), have been described in studies by Andrejczuk et al. (2008), Shima et al. (2009) and Riechelmann et al. (2012). In this approach, the motion of a great number of individual droplets within a flow field generated in LES is calculated. Turbulent mixing in such models is treated explicitly, without any parameterization. This potentially powerful approach is currently in the development stage, and further efforts are required to properly take into account processes of collisions, droplet nucleation and the formation of raindrops.

In addition to simulation of cloud fields, LES are used to develop parameterization schemes for the large scale models. Using statistical analysis of LES results (with bin microphysics), Khairoutdinov and Kogan (1999, 2000) and Kogan (2013) developed a parameterization of autoconversion and accretion rates in drizzling stratocumulus clouds as functions of droplet concentration and LWC. Kogan and Kogan (2001) derived parametrization formulas for drop effective radius in stratocumulus clouds. Wong and Ovchinnikov (2017) used LES for parameterization of subgrid-scale fluxes caused by deep convection.

In the present study we use LES results (the model details are presented below) to investigate the behavior of microphysical properties of non-precipitating and slightly precipitating shallow Cu fields under different aerosol conditions. *The goal of the study is twofold.* First, we will check the variability of effective radius in clouds of different sizes and the robustness of utilization of one mean vertical profile of $\bar{r}_e(z)$ to characterize all the clouds within the field. We explore the reasons for the comparatively low horizontal variability of effective radius despite of the high variability of LWC both within each cloud and between different clouds. Second, using the results of the LES

we propose a simple parameterization of the mean vertical profiles of effective radius and LWC that uses adiabatic LWC profile and droplet concentration at cloud base.

3. Model set-up

LES were performed using System for Atmospheric Modelling (SAM) (Khairoutdinov and Randall, 2003) with Spectral Bin Microphysics (SBM, Khain et al. 2004, 2013) (for details see webpage: <http://rossby.msrc.sunysb.edu/~marat/SAM.html>). SAM is a non-hydrostatic, inelastic model with cyclic boundary conditions in the horizontal direction. The SBM is based on solving kinetic equations for size distribution functions of water drops and Aerosol Particles (AP). Aerosols and droplet size distribution functions are defined on the doubling mass grids containing 33 bins. The drops radii range between $2\ \mu\text{m}$ and $3.2\ \text{mm}$. The size of AP serving as cloud condensational nuclei (CCN) ranges between $0.005\ \mu\text{m}$ and $2\ \mu\text{m}$. Using the values of supersaturation with respect to water the critical CCN radius is calculated (using the Köhler theory) and the APs larger than the critical size are nucleated to droplets as described by Khain et al. (2000). The rest of the AP are advected with air motion. Diffusional growth and evaporation of droplets are calculated basing on the changes in the supersaturation during a model time step. The time steps are chosen to be smaller than drop relaxation time. This is the physical condition of accurate calculation of diffusion growth/evaporation. Collision-coalescence is solved by the stochastic collision equation using the accurate method of Bott (1998). The collision kernels were calculated using an exact method described by Pinsky et al. (2001). Drop sedimentation is calculated using fall velocities determined by Beard (1976).

Fields of small trade cumulus clouds were simulated within a domain of $12.8\ \text{km} \times 12.8\ \text{km} \times 5.1\ \text{km}$ using horizontal resolution of $100\ \text{m}$, and vertical resolution of $40\ \text{m}$ with a dynamical

time step of 1 s. As a case study, small Cu observed during BOMEX were chosen for simulation (Siebesma et al., 2003). The vertical profiles of temperature and dew point used in simulations are shown in **Figure 1**. The original BOMEX profile is that with the inversion at 1500m, the other two profiles with the inversion base at 1000 m and 2000 m were used for analyzing the effect of the inversion height on the microphysical properties of simulated cloud fields.

Note that the vertical profiles of temperature and dew point shown in Fig. 1 are not specific only to the BOMEX. Similar profiles can be observed both over ocean, as well as over land at any time during warm seasons (Garratt, 1992; Jiang and Feingold, 2006).

Following Jaenicke (1988), Altaratz et al. (2008) and Ghan et al. (2011) size distribution of aerosols is designed as sum of three modes of log-normal distributions describing fine, accumulated and coarse aerosols. According to Ghan et al. (2011) typical total concentration of condensational nuclei (CN) is about 400 cm^{-3} with main fraction of this amount in the fine mode. In the simulations we used concentrations of CN within the range from 500 cm^{-3} to 5000 cm^{-3} which lead to mean droplet concentrations at cloud base of $\sim 50 \text{ cm}^{-3}$ to $\sim 500 \text{ cm}^{-3}$. According to the accepted definition, this range of droplet concentrations includes three cloud types: clean (maritime), intermediate (clean continental) and polluted (continental) (Ghan et al. 2011). Note that comparatively small mean cloud droplet concentration at cloud base at such CN concentration is determined by low vertical velocities at cloud base and by prescribed initial CN size distributions containing large fraction of small CN, which cannot be activated at such vertical velocities. We do not consider clouds developing in the extremely clean atmosphere, and producing drizzle immediately after their formation.

We will refer the simulations according to the CN concentration and inversion height: H-high, M-medium and L-low, e.g. E5000H, where E denotes “experiment” and 5000 shows CCN concentration. The list of simulations is presented in Table 1.

In addition to simulations listed in Table 1 three supplemental simulations were performed. The simulation E2000H-50 is similar to E2000H but has horizontal grid spacing of 50 m. It was performed to analyze effects of model resolution on cloud thermodynamics and microphysics. Two other simulations E2000H-RH1 and E2000H-RH2 have air relative humidity within the layer from the surface to the inversion base by 5% and 10% lower than in E2000H, respectively. The profiles of $T_d(z)$ in these simulations are shown in Figure 1. These simulations aim to investigate effects of environment humidity on cloud properties and to check universality of the parameterization proposed (see below) under different thermodynamic characteristics of the BL. Convection is triggered by random temperature perturbations at the beginning of the simulations. For isolating the aerosol effect on the thermodynamic conditions, the radiative effects (as included in the large scale forcing) as well as the surface fluxes were prescribed in all simulations (see Dagan et al., 2016 for detail). The surface fluxes and the large scale forcing of BOMEX have been used for this study following Siebesma et al. (2003).

All simulations were performed for 8.3 hours.

4. Results

4.1 Time dependencies and mean profiles

We will first examine the time evolution of the simulations in order to select the period for analysis. We have chosen the time periods when the cloud fields were quasi-stationary, i.e. the statistics and mean microphysical properties of the clouds do not change significantly with time.

Figure 2 shows time dependence of total Cloud Fraction CF (determined by the area where liquid water path is positive, i.e. calculated as a ratio of the area of the projection of the cloud on the surface to the area of the computational area) for simulations with the inversion base height of 1500 m.

Figure 2 shows that during the time period 2-6 h the changes in total CF are not significant. The moderate decrease in CF at $t > 6$ h can be attributed to thermodynamical effects of clouds on the temperature and humidity profiles in the boundary layer (Dagan et al. 2017). Hence, our analysis will be performed for the period between 2-6 h of each simulation. It allows us to relate microphysical and dynamical characteristics of the cloud fields to the initial aerosol and thermodynamic conditions. Note, that the CF increases with the decrease in CCN concentration. This behavior can be explained by more efficient evaporation of cloud droplets in polluted clouds, because of smaller droplet sizes than in cleaner clouds (Xue and Feingold, 2006).

In order to give an idea of how the cloud field simulated by SAM looks like which can simplify further interpretation of the results, we present **Figure 3** showing 3D snapshots of the LWC, N_d and r_e in E5000H. In the particular case rain water content is negligible, so LWC is equal to cloud water content (CWC), determined by cloud droplets with radii below $25 \mu m$. This is the approximate maximum drop radius that can be reached by diffusion growth and non-intense collisions between small cloud droplets (Pinsky and Khain, 2002).

The cloud field consists of clouds of different sizes and shapes.. The smallest clouds rapidly evaporate by mixing with surrounding, while few largest clouds penetrate the inversion layer. The largest clouds contain cores with high CWC. As expected, the CWC increases with height, reaching its maximum near the cloud top, while N_d is nearly constant with height. Hence, drop size, and in particular, the effective radius r_e is increasing with height, as can be seen in Fig 3c. It

is possible to see that r_e changes in horizontal direction within the range 9-11 μm in the upper parts of clouds, i.e. the relative changes of the effective radius are much lower than those of CWC and N_d .

Vertical profiles of cloud averaged cloud water content, $\overline{CWC}(z)$, rain water content, $\overline{RWC}(z)$, droplet concentration, $\overline{N_d}(z)$, and effective radius, $\overline{r_e}(z)$ of the cloud droplet mode of drop size distribution (2 μm to 25 μm), in all numerical experiments are shown in **Figure 4a-d**. Cloud averaged values are calculated as the averaged values of corresponding quantities over all clouds at any given height level.

One can see that cloud base is at about 500 m. In Fig. 4 the values of CWC, droplet concentration and effective radii were plotted at cloudy grid points with $CWC > 0.01 \text{ g m}^{-3}$, as well as $\overline{RWC}(z)$ was calculated for cloud points with $RWC > 0.01 \text{ g m}^{-3}$.

The cloud top heights are determined mainly by the location of inversion layer. Above the inversion base there is intense “cloud sorting” when smaller clouds rapidly loss their buoyancy and dissipate, so only the air in the largest clouds continues ascending. The largest clouds penetrate inversion layers by up to 500 m. At the exception of E500H and E1000H the $\overline{CWC}(z)$ increases with height. Strong increase in the $\overline{CWC}(z)$ above the inversion base is a reflection of the cloud sorting. $\overline{RWC}(z)$ is significant only in E500H (panel b).

Cloud averaged droplet concentration $\overline{N_d}$ (panel c) remains nearly constant with height in E2000, E3000 and E5000, but decreases in E500 and E1000. The reason of the decrease in \overline{CWC} and $\overline{N_d}$ in experiments with the concentration of CN of 500 and 1000 cm^{-3} can be derived from

the analysis of the profiles of \overline{RWC} and of the cloud averaged effective radius $\bar{r}_e(z)$ (panel d). One can see that in these experiments \bar{r}_e exceeds $12 \mu m$ already 500 m above cloud base. This value can be considered as the threshold value for first drizzle or raindrop formation (vanZanten et al., 2005; Benmoshe et al., 2012; Khain et al., 2013; Magaritz-Ronen et al. 2016a,b). Above this level collisions become intense, which in addition to increased mixing with the environment, leads to decrease in \overline{CWC} and $\overline{N_d}$. The values of \bar{r}_e do not exceed $20 \mu m$ even in precipitating clouds, which agrees with the estimations by Rosenfeld and Lensky (1998) who referred the regime with $\bar{r}_e \sim 20 \mu m$ to as washout regime.

Figure 5 presents the vertical profiles of the time averaged CF in different simulations. CF(z) is calculated at each model level as the ratio of number of grid points with $LWC > 10^{-5} \text{ gm}^{-3}$ to total number of grid points at the model level. The upper panel in Fig. 5 shows CF calculated using total liquid water content (LWC) including cloud and rain drops. The lower panel show CF determined by cloud droplets only.

Analysis of Fig. 5 shows the following features of the CF:

- a) CF reaches its maximum at about 200-300 m above cloud base in all simulations. Above this level, CF decreases because of evaporation of the smallest clouds, as clearly seen in **Figure 3**. Droplet evaporation in these smallest clouds makes them negatively buoyant which prevents their further growth. The strength of entrainment, which determines the maximum height of clouds is maximum in smallest clouds because smaller clouds entrain stronger due to their larger surface to volume ratio (e.g., De Rooy et al. 2013). Similar behavior of CF with height was reported in LES simulations by Siebesma et al. (2003) and observation (Nuijens et al., 2015).
- b) In the presence of inversion layer, the cloud top heights are determined largely by the height of the inversion base and does not depend on the CN concentration significantly.

c) Rain drops increase cloud cover significantly only in E500H, where rain drops increase CF above $z=1000$ m more than twice. In simulations with $CN=500 \text{ cm}^{-3}$ CF is maximum. This result can be attributed to the fact that at low droplet concentrations, the droplets are larger and do not evaporate in course of mixing with dry surrounding air as fast as small cloud droplets in polluted clouds. This effect was discussed by Dagan et al. (2017) among other. The decrease in CF with the increase in the CN concentration is a specific feature of small Cu. In case of deep convective clouds, the CF increases with the increase in the CN concentration (Khain et al, 2010, Fan et al., 2018).

Fig. 5 shows that the CF changes significantly with height. Note that in the current the operational COSMO version, the CF estimated for small (sub-grid) Cu cloud field is assumed to be independent of height and proportional to the depth of the cloudy layer. Moreover, in current NWP models including the current COSMO scheme, CF is not sensitive to aerosol loadings. This clearly contradicts the accurate LES results. The recently developed COSMO parameterization of shallow convection fluxes assumes the CF to be proportional to the mass fluxes in the cloud cores (Böing et al. 2012).

The goal of this study is to parameterize cloud-averaged profiles shown in Fig.4 for calculation of the radiative fluxes in cloud resolving models. Not all cloud layers contribute to the radiative fluxes equally. Two simplifications will be made for the following parametrizations. First, within the inversion layer, the total mass of liquid water is small because of dramatic decrease of CF with height (Fig. 5). Accordingly, we will simplify the parameterization by neglecting the contribution of liquid water within the inversion layer. Second, the formation of raindrops involves into consideration complicated microphysical processes of collisions which hinders development

of the parameterization. Accordingly, for developing the parameterization, it is of importance to evaluate the contribution of upper parts of clouds as well as rain drops to radiative cloud properties.

An important characteristic of clouds being used for estimation of their radiation properties in a short the wavelength range is optical thickness, which is related to liquid water content q_L and effective radius r_e as (Szczodrak et al., 2001):

$$\tau(z) = Q \int_z^{cloud\ top} \frac{3q_L}{4\rho_w r_e} dz', \quad (1)$$

where ρ_w is the water density, Q is the scattering efficiency. The mean scattering efficiency for cloud drops was taken equal to 2 (independently on wavelength).

Expression (1) allows calculating the vertical profile of optical thickness of a narrow cloud column within which q_L and effective radius r_e can be considered as horizontally homogeneous.

In real clouds microphysical quantities of clouds are spatially inhomogeneous. Using Eq. (1) one can calculate “effective” optical thickness $\bar{\tau}$ of the entire atmospheric layer with embedded cloud field.

The effective optical thickness that provides the same attenuation of direct radiative flux within the atmospheric layer as the attenuation calculated within each atmospheric column can be calculated as

$$\bar{\tau}(z) = -\ln \left[\frac{1}{\iint_{x,y} I_0(x,y,z_{top}) dx dy} \int_z^{z_{top}} \iint_{x,y} I_0(x,y,z_{top}) e^{-\tau(x,y,z)} dx dy dz \right], \quad (2)$$

where z_{top} is the height of the upper boundary of the layer and $I_0(x,y,z_{top})$ is the flux at this boundary, x and y are horizontal coordinates. Assuming that at the upper boundary the radiative short wavelength flux does not depend on x and y , one can get:

$$\bar{\tau}(z) = -\ln \left[\frac{1}{\iint_{x,y} dx dy} \int_z^{z_{top}} \iint_{x,y} e^{-\tau(x,y,z)} dx dy dz \right], \quad (3)$$

where τ is calculated using (1). **Figure 6** shows vertical profile of the effective optical depth averaged over 4h period (from 2h to 6h) in different simulations calculated using eq. (3). Calculations are performed over entire computational area, so contribution of cloud free regions were taken into account. Effective optical depth was calculated for cloud droplets (a) and drizzle and rain drops with radii exceeding $25 \mu m$ (b). The effective optical thickness under the simulation conditions is small because of low cloud cover. For the goals of the study, it is important that the optical thickness due to raindrops is substantially lower than that due to cloud droplets even in E500, where RWC is substantial. For higher CN concentrations contribution of raindrops to the optical depth is negligible. This result agrees well with that reported by Savijarvi et al., (1997). Savijarvi and Raisanen, (1998) showed also that contribution of raindrops to the long wave radiation fluxes is also much lower than that of cloud droplets even under strong rain rates. Moreover, consideration of RWC contribution to the optical depth would complicate the analysis without getting useful information. Therefore, we will focus below on the aerosol effects on CWC and r_e of cloud droplets.

Thin lines on Fig. 6a show the upper parts of cloud layers with contribution to the total optical depth is below than 5%. One can see that the parts of clouds penetrating the inversion layers contribute to the total optical thickness only slightly. This result will be taken into account when deriving parameterization expressions for profiles of clouds averaged quantities. Note, that the optical depth for cloud droplets is only slightly sensitive to aerosol concentration (Fig. 6a) due to low CF. The effect of aerosols is seen better in Fig. 6b because aerosols affect rain formation. Fig. 6 shows also that contribution of raindrops to optical thickness is much lower than that of cloud droplets. This small effect is explained by large effective radius of raindrops (see Eq. (1)) and low CF covered by them.

424

425 **4.2 Variability of LWC and droplet concentration**

426 **Figure 7** shows vertical changes of the CWC (panels a,c,e) and RWC (panels b,d,f)
427 occurrence in the E500H, E2000H and E5000H simulations. The cases with high inversion are
428 chosen because clouds in these cases are more developed and RWC is larger than in cases with
429 lower inversion. The color scale shows the number of cloudy grid points with specific CWC or
430 RWC plotted in logarithmic scale. Note first that significant RWC appears only in E500H above
431 2000 m. At each level on Fig. 7 a,c,e we find the grid points (in space and time) where the CWC
432 is maximal (black curves). Then on Fig. 7 b,d,f RWC is calculated in these specific grid points
433 (denoted also by black curves). Thus, the grid points of maximal CWC generally coincide with the
434 maximal RWC.

435 Brown lines denote adiabatic LWC, which represents parcels rising adiabatically from the Lifting
436 Condensation Level (LCL) assuming conversion of all water vapor in excess of saturation to liquid
437 water and neglecting collisions and drop settling. The LCL was determined by empirical formula
438 relating the LCL to the surface temperature and humidity (Bolton 1980). Simulations show that
439 this formula determines the LCL level close to that of cloud base calculated in LES. We note
440 several points in analysis of Fig. 7. First, Fig. 7 shows high variability of LWC per horizontal level.
441 At each level LWC varies from zero at cloud edges to the value relatively close to adiabatic value,
442 LWC_{ad} . This variability is caused by the competition between condensation and evaporation in
443 different locations in the clouds that are exposed to different intensities of entrainment and mixing
444 with the drier outside environment. Second, they show that there exist slightly diluted cloud
445 volumes in the lowest 1000 m above cloud base. The fraction of such slightly diluted cloud
446 volumes (grid points) with high adiabatic fraction ($AF=LWC/LWC_{ad}$) is very small and decreases

with height, as can be seen by the logarithmic scale of the plots. Note that the existence of slightly diluted cloud volumes with sizes supposedly smaller than those resolved in the simulations at such distances from cloud base was reported in high frequency in-situ measurements (see Fig. 2 in Gerber, 2000). The possible reasons of appearance of such volumes in 100-m resolution simulations are discussed in Section 6 below. Deviations of the maximum LWC from the adiabatic value LWC_{ad} increase with height. Substantial deviations of LWC from LWC_{ad} take place within the inversion layer. Note that the existence of weakly diluted cloud volumes was reported in 1 Hz frequency in-situ measurements in developing convective clouds with maximum AF values up of 0.93 at distances from 1 km to 3.4 km above cloud base (Prabha et al., 2011; Khain et al., 2013). In E500H the maximum values of sum of CWC and RWC are comparatively close to adiabatic values. Slightly diluted cloud volumes were also simulated in 100 m-resolution LES by Xue and Feingold (2006), Zhang et al. (2011), as well as in Dawe and Austin (2012).

Figure 8 presents frequency by altitude diagrams of droplet concentration for the same simulations discussed in Fig. 7. The maximum droplet concentrations in these simulations are of about 100 cm^{-3} , 420 cm^{-3} and 900 cm^{-3} , respectively. The color reflects the number of cloudy grid points with specific N_d in logarithmic scale. Black lines show droplet concentration in cloud interior in points where CWC was maximum. One can see that zones of CWC maximum are also zones of maximum droplet concentration. In E2000H and E5000H the maximum droplet concentration within the layer of 1000 m-1500 m above cloud base is nearly constant with height as could be expected in ascending adiabatic volumes. Some growth of maximum droplet concentration within the few hundred meters above cloud base is caused by in-cloud nucleation. The decrease in the droplet concentration maximum (i.e. deviation from “adiabatic” values) is

related to two mechanisms: accretion by raindrops (the most pronounced in E500H) and the effects of mixing- dilution. The first mechanism is dominating in cloud interior.

Similarly to LWC, N_d changes strongly in the horizontal direction (per height level). The dispersion of the concentration near cloud base can be attributed to fluctuations of the vertical velocities at cloud base as well as by fluctuations of LCL. The decrease in the droplet concentration values is related to the mixing process, when concentration changes from zero at cloud edge to its maximum in cloud cores.

4.3 Volume mean and effective droplet radii in cloud ensemble

Volume mean (r_v) and effective droplet (r_e) radii are among the most important microphysical characteristics of clouds. Two moment bulk schemes are able to calculate mean volume radius. At the same time radiation fluxes are calculated using effective radius. **Figure 9** shows scattering diagram r_v vs r_e as obtained in simulations E500H, E2000H and E5000H. The diagrams plotted using results of other simulations are similar to those shown in Fig. 9. The diagrams show that the values of r_v and r_e are well correlated. Note that $r_e \geq r_v$ according to definition (see Appendix 1). The 1:1 line reflects grid points with very narrow DSD where $r_e \approx r_v$, since for monodisperse DSDs $r_e = r_v$. One can see that the lower the CN concentration, the larger the maximum values of r_e and r_v . The difference between r_e and r_v increases with the increase in the DSD width. Formation of large cloud droplets in DSD by drop-drop collisions leads to larger increase in r_e than of r_v . Accordingly, the dispersion of scattering diagram r_v vs r_e increases with the decrease in the droplet (or CN) concentration.

Accordingly, in several studies the mean volume and effective radii are related as

$$r_e \approx k r_v \quad (4)$$

Freud and Rosenfeld (2012) found that in tops of non-precipitating developing deep convective clouds $k \approx 1.08$. Similar relationship was numerically found by Benmoshe et al. (2012) for deep convective clouds using the Hebrew University Cloud Model (HUCM). Measurements in stratocumulus clouds show that k varies between 1.14 and 1.21 (Reid et al., 1999; Martin et al., 1994). Using numerical results of LES of non-drizzling stratocumulus clouds, Kogan and Kogan (2001) and Magaritz-Ronen et al. (2016b) found that the effective radius is about 10% larger than the mean volume radius that agrees well with the observations.

According to our simulations $k \approx 1.15$ -1.17. Thus, our LES simulations support these observational and numerical results, showing a general character of such relationship. The lowest values of coefficient k take place for polluted clouds in which DSD are the narrowest. Accordingly, the largest values of k take place for clean clouds, where DSD width is largest, and the existence of large cloud droplets increases r_e .

Main properties of effective radius in cloud field of small Cu can be derived from **Figure 10** showing height vs. r_e scattering diagrams for selected simulations with different inversion layer heights and different aerosol concentrations. These simulations reflect the basic properties of effective radius.

Purple lines in Fig. 10 denote the profiles of “adiabatic” effective radius of cloud droplets r_{e_ad} , which could be observed in adiabatically ascending cloud volume with droplet concentration N_{d_ad} calculated at cloud base. In Fig. 10 r_{e_ad} is calculated as:

$$r_{e_ad}(z) = 1.15 \cdot r_v = 1.15 \cdot \left(\frac{LWC_{ad}(z)}{\frac{4}{3}\pi\rho_w N_{d_ad}} \right)^{1/3} \quad (5)$$

where $LWC_{ad}(z)$ is adiabatic LWC that can be calculated as described, for example, by Pontikis (1996) or Pinsky et al. (2012). The adiabatic cloud number concentration N_{d_ad} is the concentration in an adiabatic cloud core. As can be seen from Fig. 7, the cloud cores are adiabatic only at the first few hundreds of meters above the cloud base. Hence, in these levels $r_e(z)$ in the cloud cores should be equal to $r_{e_ad}(z)$. We have chosen N_{d_ad} so that $r_{e_ad}(z)$ will nearly coincide with $r_e(z)$ in the cloud cores. The values of N_{d_ad} are shown by solid brown line segments in Fig. 8. N_{d_ad} can be calculated in large scale models using, for instance, lookup tables as a function of aerosol concentration and cloud base vertical velocities (Segal and Khain, 2006), theoretical formulas (Pinsky et al. 2012) or other approaches (Ghan et al. 2011). For instance, the cloud base vertical velocities in the COSMO model are calculated as a sum of gridscale updraft, vertical component of turbulent fluctuations using turbulent kinetic energy (with isotropy assumption), radiative cooling effect (Khvorostyanov and Curry, 1999), and the convective velocity scale (Deardorff, 1970). Other NWP models calculate these velocities using the intensity of turbulence in the BL and the BL height (e.g. Zheng and Rosenfeld, 2015). In NWP models these parameters are calculated in boundary layer schemes.

Because of some uncertainties in evaluation of N_{d_ad} , we will refer r_{e_ad} to as “modeled” adiabatic effective radius. Although the N_d and LWC in cloud cores become with height smaller than N_{d_ad} and LWC_{ad} , respectively, r_{e_ad} still represents well the effective radius in cloud cores. The advantage of r_{e_ad} is that it can be calculated in any model knowing the LCL (together with the cloud base temperature and pressure) and the droplet concentration at cloud base.

An analysis of Fig. 10 shows several important features of effective radius in clouds forming in cloud fields:

a) Strong effect of aerosols

A well-known effect is the faster effective radius growth with height in case of low CCN concentrations. In case of clean environment, N_d is small, therefore the fewer droplets that form near cloud base have little competition on the available supersaturation (S_w) (Pinsky et al. 2012, 2014; Dagan et al. 2016). As a result, S_w remains relatively high and the droplets (and their effective radius) grow rapidly with height. At CN concentration of 5000 cm^{-3} , the maximum of the effective radius remains below $13\text{-}15 \mu\text{m}$, so these clouds do not produce neither raindrops nor drizzle. At CN concentration of 2000 cm^{-3} , the maximum effective radius reaches $14\text{-}15 \mu\text{m}$ at $z=2000\text{m}$. So, light drizzle arises above this level (Fig. 7). In E500 the maximum of r_e exceeds $15 \mu\text{m}$ and raindrops arise (Fig. 7). The reason of the existence of critical or the threshold value of effective radius is discussed in several studies (Freud and Rosenfeld, 2012; Pinsky and Khain, 2002; Benmoshe et al, 2012; Khain et al., 2013; Magaritz-Ronen et al. 2016b). Long (1974) showed that collision kernel for small droplets is proportional to the six power of droplet radius. Freud and Rosenfeld (2012) evaluated that the collision kernel as proportional to r_e^5 . These evaluations show dramatic increase in the rate of collisions when the largest cloud droplets reach the radii of $20\text{-}21 \mu\text{m}$, which correspond to the critical value of effective radius mentioned above.

b) Low horizontal variability of effective radius

A fundamental property of effective radius is low horizontal variability. This variability is much lower than that of LWC as seen in Fig. 7. The variability of effective radius is relatively

553 large near cloud base. This can be attributed to the fact that r_e rapidly grows above the LCL, so
 554 even small local fluctuations of LCL lead to significant fluctuations of effective radius at low
 555 levels. Generally, the averaged (over all heights) relative variability varies between 10-15%. This
 556 result is in agreement with observations in small cumulus clouds (Arabas et al. 2009; Gerber et al,
 557 2008; Schmeissner et al. 2015) and in deep convective clouds (Prabha et al. 2011; Khain et al,
 558 2013). In addition, low variability in deep non-precipitating clouds under different geographical
 559 locations observed in-situ was reported previously (Tas et al, 2012, 2015; Liu and Daum, 2000,
 560 Freud and Rosenfeld, 2012; Rosenfeld et al., 2014). Rosenfeld et al. (2016) used the low variability
 561 of r_e found in observations to propose a method to determine CCN concentration in the boundary
 562 layer. Note that the low variability of r_e in small cumuli should be considered as somehow
 563 surprising, since the influence of mixing with environment is more significant than in large deep
 564 convective clouds and in a horizontally homogeneous Sc. Schmeissner et al. (2015) stress that
 565 despite the fact that in dissolving small Cu at their dissipating stage LWC and droplet concentration
 566 are decreased by about 50% compared to growing Cu, droplet size remains almost constant. Our
 567 LES reproduce these observation findings. Schmeissner et al. (2015) found also that some fraction
 568 of DSD are bi-modal because of incloud nucleation. SAM microphysics obviously takes into
 569 account all the mechanisms leading to incloud nucleation and bi-modal DSD formation. However,
 570 as mentioned above, our results show low variability of r_e . We partially attribute this insensitivity
 571 to the following. The mean volume radius is proportional to $(LWC/Nd)^{1/3}$. As the incloud
 572 nucleation leads to formation of smallest droplets, the LWC is defined by the first mode of droplets
 573 activated at cloud base. Because of the 1/3 power, the incloud nucleation cannot change Nd
 574 strongly enough to affect the mean volume radius (as well as r_e) significantly.

Low variability of r_e indicates that cloud field can be characterized by robust vertical profile of effective radius that is close to the adiabatic one and depends on the aerosol loading.

c) The maximum effective radius is in cloud interior

The important feature is that the effective radius is maximal in cloud interior (black lines), where LWC are maximum. In cloud cores the profiles of $r_e(z)$ almost coincide with the adiabatic values (purple lines) calculated according Eq. (5). This fact shows that cloud droplets reach maximum size in cloud cores, together with the maximum LWC and the maximum droplet concentration.

d) limiting value in case of raindrop formation

As seen in fig. 10, r_e in cloud core in simulations with $CN=500\text{ cm}^{-3}$ is maximum in cloud cores and close to the adiabatic value. Formation of raindrops is seen by termination of the r_e growth with height. In case of rain drop formation, effective radius determined within the range of cloud droplet radii ($<25\text{ }\mu\text{m}$) does not exceed about $22\text{ }\mu\text{m}$ and remains height independent (Fig. 10, E500H). Such regime is known as rainout (Rosenfeld and Lensky, 1998). The reason of low dependence of r_e with height in case of raindrop formation is that raindrops collect cloud droplets of all sizes that leads to decrease in droplet concentration, but does not change effective radius of the cloud droplet mode.

According to the results, in case of rain formation, the maximum r_e of cloud droplets can be calculated as:

$$r_{e_{max}} = \min(22\mu\text{m}, r_{e_{ad}}) \quad (6)$$

Because of low variability of r_e , the values of r_e are concentrated around $\overline{r_e}$, which is slightly smaller than r_{e_ad} .

The physical reasons of low variability of effective radius were analyzed by Pinsky et al. (2016b) and Pinsky and Khain (2018a) using a semi-analytical diffusion-mixing model and by Magaritz-Ronen et al. (2016b) who used a Lagrangian-Eulerian model of Sc with a precise description of microphysical processes of diffusion growth and turbulent mixing. Relative humidity in cloudy volumes, even well diluted ones, remains high which does not allow effective radius to decrease anyhow significantly. Small decrease in r_e reflects the contribution of air volumes newly penetrating clouds and located near cloud edges, as was observed by e.g. Kumar et al. (2017). In such volumes partial evaporation of drops penetrating from cloudy volumes leads to formation of DSD with lower effective radii. Rapid increase of relative humidity in such volumes with time leads to termination of evaporation of largest droplets penetrating from the cloudy volumes. As a result, the effective radius in the volumes penetrating clouds rapidly reaches values typical of cloudy volumes, while LWC and droplet concentration remain much lower than in the cloud core. This process of rapid increase of r_e till the value close to that of cloud interior is investigated in detail by Pinsky et al. (2016b), Magaritz-Ronen et al. (2016b) and Pinsky and Khain (2018a). Note that turbulent mixing leads to formation of a humid shell of a moist air around the cloud (Heus and Jonker 2008; Lehmann et al., 2009; Bar-Or et al., 2012; Schmeissner et al., 2015; Pinsky and Khain, 2018a). The mixing with humid air, which entrains clouds, does not cause strong changes in drop sizes near cloud edge.

5. Parameterization of microphysical parameters of cloud ensembles

For practical goals, it is desirable to characterize cloud field by some mean vertical profile $\overline{r_e}(z)$. Analysis of results presented in Fig. 10 shows that $\overline{r_e}(z)$ is smaller than the maximum value $r_{e_ad}(z)$ only by ~10-15%. The difference between $\overline{r_e}(z)$ and $r_{e_ad}(z)$ reaches its maximum at the inversion base level. This increase is related to the fact that cloud ensemble contains clouds of different size and clouds of lower width experience stronger effects of mixing because the interface zone affected by mixing in such clouds occupies a significant fraction of the cloud volume. Above the base of inversion the difference $r_{e_ad}(z) - \overline{r_e}(z)$ decreases again, since only largest clouds remain. This behavior retards simple approximation of $\overline{r_e}(z)$ via $r_{e_ad}(z)$. We will approximate dependence between these two quantities (as well as other approximation of averaged values) ignoring the upper part of clouds within inversion layer, which contribution to the optical depth of cloud layer is less than 5% (see Fig. 6a). Within the layer below inversion base the cloud averaged effective radius can be approximated as

$$\overline{r_e}(z) = \alpha(z)r_{e_ad}(z) \quad , \quad (7)$$

where $\alpha(z) = 0.95 - 1.2 \cdot 10^{-4}(z - z_{cb})$, where z is in meters,

where z_{cb} is the cloud base level, determined by the minimal distance from the surface where supersaturation for the first time becomes positive and droplet nucleation takes place. In order to take into account the effect of raindrops, the values of $r_{e_ad}(z)$ in Eq. (7) were replaced by $r_{e_max}(z)$ calculated using Eq. (6). According relation (7), $\overline{r_e}(z)$ is closer to $r_{e_ad}(z)$ than as reported by Gerber et al. (2008). We attribute this to different approaches to define N_{d_ad} and hence $r_{e_ad}(z)$

(see comments to eqn. 5). At the same time, the values of $\overline{r_e}(z)$ correspond well to Gerber et al. (2008) (tables 2,3 therein).

Vertical profiles of the cloud averaged effective radius calculated directly from LES and parameterized using Eqs. (5-7) are shown in **Figure 11**.

One can see a good agreement of parameterized $\overline{r_e}(z)$ with those calculated directly in the LES within entire range of aerosol loadings and different levels of the inversion. Standard deviation is of $0.39 \mu m$.

The next step is parameterization of mean droplet concentration as function of droplet concentration at cloud base that, as was mentioned above, can be determined using different approaches in different kind of atmospheric models, including NWP models. The concentration at cloud base can be referred to as adiabatic concentration N_{d_ad} , which being formed at cloud base does not change with height within ascending adiabatic parcels (in small Cu the changes of air density with height are small). Profiles of $\overline{N_d}(z)$ depend on whether clouds produce raindrops or not. In case of non-precipitating clouds $\overline{N_d}(z)$ and N_{d_ad} are equal to the maximum value N_{d_max} , which can be considered as constant with height. Analysis of Fig. 8 shows that the maximum droplet concentration in clouds producing raindrops can be approximated as a constant till the level at which $r_{e_ad} = 12 \mu m$ and linearly decreasing above this level. Statistical analysis shows that the profile of maximal droplet concentration can be written in the form

$$N_{d_max}(z) = \begin{cases} N_{d_ad}, & \text{below the level } z_{12}, \text{ where } r_{e_ad} = 12 \mu m \\ N_{d_ad}[1 - \gamma(z - z_{12})], & \text{above the level } z_{12} \end{cases} \quad (8)$$

where $\gamma = 0.45 m^{-1}$ and z is in meters.

$$\overline{N_d}(z) \approx \beta N_{d_max}(z), \quad (9)$$

where on average (over all heights and simulations) $\beta = 0.38$ with standard deviation of 0.03.

The parameters in expressions (7-9) are obtained minimizing the root mean square over all the simulations. Expressions (8) and (9) allow to calculate the averaged concentration profiles using the droplet concentration at cloud base and the height of the level where r_{e_ad} reaches the precipitating threshold.

Figure 12 shows profiles of cloud averaged droplet concentration obtained in LES and using expressions (8) and (9). One can see a good agreement between the approximations and profiles directly calculated using LES.

In addition to $\overline{r_e}(z)$, the parametrizations of radiation transfer through unresolved cloudiness in many NWP and climatic models require a prognostic calculation of $\overline{LWC}(z)$. As mentioned in the introduction, the $\overline{LWC}(z)$ of unresolved clouds in the COSMO model is currently crudely parameterized as a function of the temperature. Now, using the parametrization of $\overline{r_e}(z)$ and $\overline{N_d}(z)$ as mentioned above, we are able to parametrize $\overline{LWC}(z)$ as well. Strictly speaking, the practically required values of $\overline{LWC}(z)$ should be determined as:

$$\overline{LWC}(z) = \overline{\frac{4}{3}\pi\rho_w N_d(z) r_v^3(z)} = \overline{\frac{4}{3}\pi\rho_w N_d(z) \left(\frac{r_e(z)}{1.15}\right)^3} \quad (10)$$

However, since variability of effective radius is low, the last equality can be rewritten as:

$$\overline{LWC}(z) \approx \frac{4}{3}\pi\rho_w \overline{N_d}(z) \left(\frac{\overline{r_e}(z)}{1.15}\right)^3, \quad (11)$$

which is substantially simpler than Eq. (10).

Figure 13 presents the vertical profiles of $\overline{LWC}(z)$ calculated directly from the results of the LES simulations and the profiles of $\overline{LWC}(z)$ calculated using Eq. (11).

One can see that eq. (11) allows reproducing the LES profiles of $\overline{CWC}(z)$ quite accurately, especially in comparison with COSMO approximations (cyan solid and dashed lines). Deviations of CWC calculated using Eq. (11) from that calculated directly in LES seen at higher levels are not of high importance for calculation of radiation fluxes because CF of these clouds at such altitudes are low (see Fig. 5).

In order to evaluate the errors in calculation of optical depth using the approximation formulas (7) and (11) instead of the averaged values calculated in LES we present **Figure 14**. The figure shows vertical profiles of the optical depth calculated by formula (1) using the approximation expressions and the average values calculated directly in LES. One can see a very good agreement in the approximation and directly calculated values.

We would like to stress that calculation of optical depth of cloud layer requires the utilization of more complicated procedure than just application of Eq. (1), but a good agreement of vertical profiles of optical depth seen in Fig. 14 indicates that approximated formulas are accurate enough to be applied in such calculations.

6. Comparison with observations and sensitivity analysis

Our parameterization aims to reproduce first of all the average vertical profiles of effective radius and of LWC. Accordingly, we first compare the vertical profiles of these values with in-situ observations in small Cu.

The grid spacing of 100 m x 100 m x 40 m used in this study was applied also by Siebesma et al. (2003), Neggers et al. (2003), Xue and Feingold (2006), Zhang et al. (2011) and Heiblum et al. (2016a,b), who showed that this grid spacing is suitable for simulation of main properties of small cumulus. To evaluate the role of grid spacing, we present also results of E2000H-50 with the horizontal grid spacing of 50 m (see Section 3). **Figure 15** shows vertical profiles of cloud averaged r_e obtained in simulations E5000H, E2000H, E2000H-50, E500H, which differ by aerosol concentrations. The mean values of r_e obtained during in-situ measurements in polluted atmosphere in GoMaCCS in (Jiang et al, 2008; Lu et al., 2008), in CARRIBA (Schmeissner et al., 2015) and in RICO (Gerber et al. 2008; Arabas et al., 2009) are presented for comparison. Note that N_d in E5000H ($\sim 380 \text{ cm}^{-3}$) was slightly lower than the observed in GoMaCCS (about 500 cm^{-3}) which explains slightly larger r_e in E5000H. The values of N_d in E2000H, E2000H-50 ($110\text{-}130 \text{ cm}^{-3}$) were similar to those observed during CARRIBA ($70\text{-}135 \text{ cm}^{-3}$) and slightly larger than in flight RF12 during RICO ($54\text{-}116 \text{ cm}^{-3}$) (Gerber et al., 2008). Accordingly, r_e in these simulations is in an excellent agreement with that in CARRIBA and is slightly smaller than that in RICO. N_d in E500H and in flight RF07 during RICO was below 50 cm^{-3} (Arabas et al., 2009). Again, there is an excellent agreement between results of simulations and observations. In flights RF06, RF09 and RF012 N_d was 2-3 times larger than in RF07. Consequently, r_e values in these flights were smaller and close to those simulated in E2000H (blue line in Fig. 15). Note that the profiles of mean $r_e(z)$ in E2000H, E2000H-50 actually coincide, showing low sensitivity to the grid spacing changes.

Note that r_e is the most robust value having low horizontal variability. Other variables experience larger variability. **Figure 16** presents comparison of averaged LWC simulated using SAM with observations. It also compares the profiles of averaged LWC obtained in simulations with horizontal resolutions of 100 m vs. 50 m (E2000H and E2000H-50, respectively). Note first, that profiles obtained using resolutions of 50 m and 100 m are very close. These results may indicate that mean profiles of LWC are determined by motions with scales of 100 m or larger. Consequently, resolution (at least within the range of 50-100 m) does not play an important role.

As mentioned by Jiang et al. (2008), “owing to the human element, aircraft sampling biases are inherently difficult to evaluate”. Besides human element, cloud averaged LWC depends on many factors, including the minimum LWC value that is chosen to define cloud edge; the criteria of the choice of clouds for statistical analysis of observations (see for example Raga et al., 1990; Gerber et al., 2008); etc. Modern probes have different detectable levels of LWC from 0.002 g/m^3 (PVM) to about 0.05 g/m^3 (the King probe). Katzwinkel et al. (2014) define cloud as the region with $\text{LWC} > 0.2 \text{ gm}^{-3}$ in order to separate cloud interior from the interface zone. Raga et al. (1990) and Gerber et al. (2008) have chosen clouds with significant updrafts, in which vertical velocities are positive in at least 80% of the Cu traverse. Moreover, Cu are typically traversed near cloud tops.

Following Bar-or et al. (2012), Tas et al. (2015), Dagan et al. (2015, 2016) and many other studies, we used the threshold of minimum LWC of 0.01 gm^{-3} (which corresponds to about 10 small droplets per cm^3) to determine the cloud averaged LWC profile. This is in agreement with the criteria of Deng et al. (2009) for the determination of a cloudy region. Fig. 16 also shows profiles of averaged LWC obtained using the criteria of cloud as $\text{LWC} > 0.05 \text{ gm}^{-3}$ which was used, for instance, by Abel and Shipway (2007) and Jiang et al. (2008). One can see that the choice of

the larger threshold leads to small increase in LWC. Note that utilization of 50 m resolution instead of 100 m changes the mean LWC profile even smaller.

In general, the comparison with the observations shows that the model reproduces the averaged LWC quite reasonably.

Note that the distributions of vertical velocity are in agreement with observations and AF values increase with vertical velocity (not shown). These results agree with that observed by Schmeissner et al. (2015) who showed that the values of AF are larger in developing Cu, characterized by larger vertical velocity. **Figure 17** shows PDF of 90th percentile of the AF and vertical velocity within clouds in CARRIBA measurements (Katzwinkel et al., 2014) and in E2000H simulation around height of 1500m. The measurements were performed ~100 m below cloud tops, with effective resolution of 20 cm. E2000H simulation results are presented for heights of 1380-1540 m.

One can see that the 90th percentiles are distributed similarly in measurements and the simulation. More cases with larger AF and W in E2000H can be attributed to slightly different stratifications and filtering out the largest Cu in measurements.

Comparison of Fig. 7 and Fig. 17 with corresponding figures obtained from high frequency in-situ measurements: fig. 2 from Gerber (2000), fig. 1 from Gerber et al. (2008) and fig. 3 from Katzwinkel et al. (2014) show surprising similarity between simulations and high frequency observations. It is clear that 100m-resolution numerical results cannot be directly compared with high resolution measurements of 10-20 cm. Such high resolutions are not available in any cloud model including Lagrangian models mentioned above. However, both simulations and measurements indicate the existence of slightly diluted cloud volumes at comparatively high altitudes. We interpret this similarity as follows:

a) Fig. 1 from Gerber (2000) and fig. 5.34 from (Wendish and Brenguier, 2012, Chapter 5) show that width of high AF zones can be of the order of 100 m, which can be detected by the LES. We attribute the existence of such zones to the fact that the most energetic LWC fluctuations are related to energetic W fluctuations with scales of order of 100 m or larger (Magaritz-Ronen et al., 2014). We believe that PDF of W in Fig. 17c is determined by such large fluctuations.

b) Statistics available in the model is much larger than in measurements. Since the fraction of cloud volumes with high AF is very small at high levels, in-situ measurements can miss such volumes, while model detects all such volumes.

c) In-situ measurements often performed near cloud tops, where AF is small. Moreover, typically they avoid measurements in invigorous clouds. AF is calculated either by averaging over clouds or over wide zones with $W > 0$ (Lu et al., 2008). Such averaging masks the possible existence of large values of AF. As a result, the measurements may miss by one or another reason the volumes with high AF. In contrast, model detects all such volumes.

So, we believe that 1-Hz in-situ measurements underestimate the number of volumes with high AF. This underestimation is partially compensated by using high frequency measurements (Gerber, 2000; Gerber et al., 2008; Katzwinkel et al., 2014, Schmeissner et al., 2015). As a result, we obtain these surprising similarities of AF and LWC profiles with high frequency measurements. Note that in any case the amount of high AF volumes at high levels is so small that they do not affect averaged profiles of corresponding values.

In several studies (e.g. Stevens and Seifert, 2008; Seifert and Heus 2013; Seifert et al. 2015) the importance of environmental air humidity on clouds as well as on the structure of cloud fields was reported. To show that the parameterization proposed remains suitable for another

environmental RH, two sensitivity runs E2000H-RH1 and E2000H-RH2 (see Section 3) were performed with RH decreased by 5% and 10%, respectively, in the layer from the surface to the inversion base. **Figure 18** shows average r_e profiles of E2000H, E2000H-RH1, E2000H-RH2 and E2000H-50. Similarly to Fig. 11, the parameterized profiles are also presented using Eqs. (5-7).

One can see that clouds are lower and cloud bases are higher with the decrease in RH. Despite the significant changes in the cloud structure, the parameterization using Eqs. (5-7) works well. The 50 m resolution averaged r_e profile almost coincides with that of 100 m.

We see therefore that the proposed parametrizations for mean profiles of r_e (Fig. 11) and LWC (Fig. 13) are robust as regards to model resolution, thermodynamical conditions and aerosol concentrations.

7. Discussion and conclusions

Small Cu are still subgrid phenomena for large scale NWP models and even for CRM. Taking into account the important role of small Cu in radiation budget and in BL structure, there is a strong necessity to parameterize their effects in such models. Consequently, we need to characterize the cloud field by comparatively small number of governing parameters that can be used in large scale models. Among such parameters are effective radius and LWC.

The goal of the study was two-fold: a) Showing the robustness of characterizing all the clouds within the field by one mean vertical profile of effective radius $\bar{r}_e(z)$. b) Proposing a parameterization of the mean vertical profiles of r_e and LWC in small warm Cu.

To accomplish the goal, the fields of small Cu in unstable boundary layer below an inversion were simulated using SAM with spectral bin microphysics. LES were performed for different thermodynamic conditions and wide range of aerosol concentrations.

The main results can be formulated as follows.

a) Despite the high variability of LWC and droplet concentration within clouds and between different clouds, the mean volume and effective radius of droplets per specific level vary only slightly. This indicates similarity of DSDs along the horizontal direction within clouds and between different clouds. Such similarity with the unchanged modal radius of DSD was reported in in-situ observations in Cu (Paluch and Knight, 1984; Paluch, 1986; Gerber 2000; Gerber et al., 2008; Paluch and Baumgardner, 1989; Prabha et al, 2011). Low variability of r_e is a consequence of the facts that the mixing within clouds and at cloud edges is inhomogeneous and that the entrained air is humid (Pinsky and Khain, 2018a). Theoretical and numerical studies with spectral bin models also show that the polydispersivity of droplet size distributions substantially decreases the variability of effective radius during mixing (Pinsky et al., 2016a; Pinsky and Khain, 2018b). Thus, even intense mixing and strong dilution typical of small Cu do not increase the variability of r_e significantly. These findings allow to characterize the cloud field by a specific vertical profile of $\bar{r}_e(z)$.

Note, that inhomogeneous and homogeneous mixing types are separated by scales less than one meter (Pinsky et al., 2016a). This fact brings up the question – why are spectral microphysics models with resolution of 100 meter able to reproduce observed DSD and their moments? Pinsky et al., 2016a showed that the microphysical quantities in clouds are not sensitive to that separation scale if the model grid spacing is less than the spatial radius of correlation of microphysical quantities in clouds, which is of order of 150-250m.

b) We have used LES to parametrize the vertical profiles of $\bar{r}_e(z)$ and $\overline{LWC}(z)$ for different aerosol concentrations and thermodynamical conditions. Assuming that N_d at cloud base can be deduced from the CCN concentration (e.g. Segal and Khain, 2006), the adiabatic mean volume

831 radius profile was calculated using the theoretical profile of LWC_{ad} . Using the found relation
832 between r_v and r_e , we deduced the adiabatic profile $r_{e_ad}(z)$. $r_{e_ad}(z)$ was then used to parametrize
833 $\bar{r}_e(z)$ assuming increased effect of mixing with height. We have parametrized $\overline{N_d}(z)$ in terms of
834 N_d at cloud base taking into account decrease of N_d with height in cases of drizzle formation.
835 $\overline{LWC}(z)$ was then parametrized using $\overline{N_d}(z)$ and $\bar{r}_e(z)$ assuming low variability of r_e in horizontal.

836 c) Universality of the parameterization formulas was justified in LES with different grid
837 spacing (100m and 50m) and different environmental humidity, as well as by detailed comparison
838 with in-situ measurements (Gerber, 2000; Gerber et al., 2008; Abel et al., 2007; Lu et al., 2008;
839 Jiang et al., 2008; Arabas et al., 2009; Katzwinkel et al., 2014; Schmeiser et al. 2015). The
840 universality follows from the fact that the parameterized values depend only on the adiabatic
841 values, which are universal.

842 Thus, we suppose that the parameterization formulas derived in this study are suitable for non-
843 precipitating warm Cu developing under wide range of thermodynamic and aerosol conditions.
844 For example, transition from maritime to continental conditions is partially described by increase
845 in CCN concentrations. BL diurnal cycle is partially described by changes in inversion height and
846 accordingly of cloud depth. When implemented into NWP models, the parametrization specific
847 values would adjust themselves continuously in space and time (depending on local cloud base
848 and inversion heights, temperature and CCN concentration in the model). We believe therefore,
849 that these parameterization profiles can be used for calculation of radiation properties of Cu fields
850 in large scale models. That will allow better estimation of optical properties and radiation transfer
851 through such clouds. High sensitivity of microphysical parameters to aerosols indicate the
852 necessity to determine better aerosol concentrations in large scale models, including NWP ones.
853 For sake of more generality, it is worthwhile to test the proposed parameterizations for different

temperatures and Bowen ratios (Zhang et al., 2017) in future study. In addition to LWC and r_e , the cloud cover of small Cu fields and vertical overlap of cloudy layers should be parametrized in a future study.

At the end of the discussion section we would like to address the role of adiabatic processes in formation of the universal profiles of effective radius $r_e(z)$ and in first rain drop formation.

a) As was mentioned above, the values of $r_e(z)$ are close to those that can be obtained in adiabatically ascending parcel. We do not see any mechanism, which could lead to such universal profile except the dominating adiabatic ascent. As was shown in Fig. 7 and 17, LES indicate existence of adiabatic or diluted only slightly cloud volumes up to heights of 1-1.5 km above cloud base. Mixing of such volumes with surrounding does not lead to change in r_e even in the dilution zone. The effective radius decreases only within a narrow zone of a few tens of meters at cloud edges (Pinsky and Khain, 2018a). Because of the low width of these zones the cloud averaged r_e do not differ much from its maximum adiabatic value.

b) According to our simulations, cloud volumes (grid points) with maximum LWC contain the maximum number concentration. Technically, we have first found the time-space coordinates with maximum LWC, and then marked them on the RWC, r_e and N_d scatter-plots (figs. 7b, 8 and 10, respectively). It means that the collision rate in these volumes is maximum. It allows assuming that first raindrops form in cloud volumes, where dilution with surrounding is minimal.

Earlier such findings were reported in LES by Seifert et al. (2010) for trade wind Cu, and by Benmoshe et al. (2012) and Khain et. al. (2013) for developing deep convective clouds. Formation of raindrops in slightly diluted cores explains a success of dynamically simple 1-D parcel models in prediction of the conditions and the height of the first rain drops formation (Pinsky et al. 2002; Freud and Rosenfeld, 2012). Therefore, the results indicate dominating role of basic adiabatic

processes in cloud's cores in formation of microphysical cloud structure. We found that this conclusion is valid even in small Cu, although the mixing there is very significant (because of the big surface-area to volume ratio).

Note, that although not analyzed in this study, other mechanisms of rain formation are also discussed in literature. Among them are the effects of giant and ultra-giant CCN (Baker et al., 1980 and Blyth et al. 2003); decrease in droplet concentration in course of inhomogeneous mixing leading to more intense diffusional growth and formation of superadiabatic droplets (Devenish et al. 2012); and turbulence-induced collision rate enhancement (Pinsky et al., 2008; Wang and Grabowski, 2009; Seifert et al., 2010; Benmoshe et al., 2012; Hoffmann et al., 2017). Grabowski and Abade (2017) investigated DSD broadening in turbulent flow in course of diffusional growth. Hence, more studies are required to establish the mechanisms of rain formation in Cu.

Acknowledgements.

The authors express their gratitude to M. Ovchinnikov for support with SAM. The study is performed within the Test and Tuning of Revised Cloud Radiation Coupling (T²RC²) Project of the COSMO consortium. Scientific group of The Hebrew University of Jerusalem is supported by the U.S. Department of Energy Atmospheric System Research program (grant DE-SC0014295, DE-FOA-0001638) and The Israel Science Foundation (grants 1393/14 and 2027/17). Scientific group of The Weizmann Institute of Science has been supported by the Minerva foundation with funding from the Federal German Ministry of Education and Research.

Appendix 1. Relationship between mean volume and effective radius

899 According to definition, the expressions for effective radius r_{eff} and mean volume radius r_v
 900 are:

$$901 \quad r_{eff} = \frac{\int_{r_{min}}^{r_{max}} r^3 f(r) dr}{\int_{r_{min}}^{r_{max}} r^2 f(r) dr} \quad (A1)$$

$$902 \quad r_v = \left(\int_{r_{min}}^{r_{max}} r^3 f(r) dr \right)^{1/3} \quad (A2)$$

903 where $f(r)$ is DSD with normalization $\int_{r_{min}}^{r_{max}} f(r) dr = 1$. This DSD can be interpreted as

904 probability distribution function at $r \geq 0$. The ratio $\gamma = \frac{r_v}{r_{eff}}$ can be written as

$$905 \quad \gamma = \frac{r_v}{r_{eff}} = \frac{\int_{r_{min}}^{r_{max}} r^2 f(r) dr}{\left(\int_{r_{min}}^{r_{max}} r^3 f(r) dr \right)^{2/3}} \cdot \quad (A3)$$

906 According to Inequality for absolute moments (see Korn and Korn, 2000):

$$907 \quad \left(\int_{r_{min}}^{r_{max}} |r|^k f(r) dr \right)^{1/k} \leq \left(\int_{r_{min}}^{r_{max}} |r|^{k+1} f(r) dr \right)^{1/(k+1)} \quad (A4)$$

908 In particular for $k=2$, since $r \geq 0$ $\left(\int_{r_{\min}}^{r_{\max}} r^2 f(r) dr \right)^{1/2} \leq \left(\int_{r_{\min}}^{r_{\max}} r^3 f(r) dr \right)^{1/3}$. This inequality and Eq.

909 (A3) lead to the following inequality $\gamma = \frac{\int_{r_{\min}}^{r_{\max}} r^2 f(r) dr}{\left(\int_{r_{\min}}^{r_{\max}} r^3 f(r) dr \right)^{2/3}} \leq 1$, which means that $r_v \leq r_{eff}$.

910

911 References:

912 Abel, S. J. and B. J. Shipway, 2007: A comparison of cloud-resolving model simulations of
 913 trade wind cumulus with aircraft observations taken during RICO. *Q. J. R. Meteorol. Soc.* 133:
 914 781–794.

915 Albrecht B., 1989: Aerosols, cloud microphysics and fractional cloudiness. *Science*, 245,
 916 1227-1230.

917 Altaratz, O., I. Koren, T. Reisner, A.B. Kostinski, G. Feingold, Z. Levin, and Y. Yin, 2008:
 918 Aerosols' influence on the interplay between condensation, evaporation and rain in warm cumulus
 919 cloud, *Atmos. Chem. Phys.*, 8(1), 15-24, doi: 10.5194/acp-8-15-2008.

920 Andreae, M. O., Rosenfeld, D. Artaxo, P. Costa A. A., Frank G. P., Longo K. M., and Silva-
 921 Dias M. A. F., 2004. Smoking rain clouds over the Amazon. *Science*, 303, 1337-1342.

922 Andrejczuk, M., Reisner, J.M., Henson, B., Dubey, M.K. and Jeffery, C.A., 2008: The
 923 potential impacts of pollution on a nondrizzling stratus deck: Does aerosol number matter more
 924 than type? *Journal of Geophysical Research: Atmospheres*, 113(D19).

925 Arabas, S., H. Pawlowska, and W. W. Grabowski, 2009: Effective radius and droplet spectral
 926 width from in-situ aircraft observations in trade-wind cumuli during RICO, *Geophys. Res. Lett.*,

927 36(11), L11803, doi:10.1029/2009GL038257.

928 Baker, M., R. G. Corbin, and J. Latham, 1980: The influence of entrainment on the evolution
929 of cloud drop spectra: I. A model of inhomogeneous mixing. *Quart. J. Roy. Meteor. Soc.*, 106,
930 581–598.

931 Bar-Or, R. Z., I. Koren, O. Altaratz and E. Fredj, 2012: Radiative properties of humidified
932 aerosols in cloudy environment. *Atmos. Res.*, 118, 280-294.

933 Beard, K.V., 1976: Terminal velocity and shape of cloud and precipitation drops aloft. *J.*
934 *Atmos. Sci.* 33, 852-864.

935 Benmoshe N., M. Pinsky, A. Pokrovsky and A. Khain, 2012: Turbulent effects on
936 microstructure and precipitation of deep convective clouds as seen from simulations with a 2-D
937 spectral microphysics cloud model. *J. Geophys. Res.*, 117, D06220, doi:10.1029/2011JD016603.

938 Blahak, U. and Ritter, B., 2013: Towards revised cloud radiation coupling for the COSMO
939 Model, COSMO/CLM User Seminar, 5-8 March, Offenbach, Germany.

940 Blyth A. M., S. G. Lasher-Trapp, W. A. Cooper, C. A. Knight, J. Latham, 2003: The role of
941 giant and ultragiant nuclei in the formation of early radar echoes in warm cumulus clouds. *J.*
942 *Atmos. Sci.*, 60, 2257-2272.

943 Böing, S. J., A. P. Siebesma, J. D. Korpershoek, and H. J. J. Jonker (2012), Detrainment in
944 deep convection, *Geophys. Res. Lett.*, 39, L20816, doi: 10.1029/2012GL053735.

945 Bolton, D., 1980: The computation of equivalent potential temperature. *Mon. Wea. Rev.*, 108,
946 1046–1053.

947 Bony, S. and Dufresne, J. L. 2005: Marine boundary layer clouds at the heart of tropical cloud
948 feedback uncertainties in climate models. *Geophysical Research Letters* 32(20).

Bott, A., 1998: A flux method for the numerical solution of the stochastic collection equation. J. Atmos. Sci., 55, 2284–2293, doi:10.1175/1520-0469(1998)055<2284:AFMFTN>2.0.CO;2.

Dagan, G., I. Koren, and O. Altaratz, 2015: Competition between core and periphery-based processes in warm convective clouds—from invigoration to suppression. Atmospheric Chemistry and Physics 15, 2749–2760.

Dagan G., I. Koren, O. Altaratz, and RH. Heiblum, 2016: Aerosol effect on the evolution of the thermodynamic properties of warm convective cloud fields. Sci. Rep. 6, 38769; doi:10.1038/srep38769.

Dagan G., I. Koren, O. Altaratz, and RH. Heiblum, 2017: Time dependent, non-monotonic response of warm convective cloud fields to changes in aerosol loading. Atmos. Chem. Phys., 17, 7435-7444, <https://doi.org/10.5194/acp-17-7435-2017>.

Dawe, J. T. and P. H. Austin, 2012: Statistical analysis of an LES shallow cumulus cloud ensemble using a cloud tracking algorithm. Atmos. Chem. Phys., 12, 1101-1119, doi: 10.5194/acp-12-1101-2012.

Deardorff, W. J.: Preliminary results from numerical integrations of the unstable boundary layer, J. Atmos. Sci., 27, 1209–1231, 1970.

De Rooy W. C., P. Bechtold, K. Frohlich, C. Hohenegger, H. Jonker, D. Mironov, A. P. Siebesma, J. Teixeira and J.-I. Yano, 2013: Entrainment and detrainment in cumulus convection: an overview, Q. J. R. Meteorol. Soc. 139: 1–19.

Deng, Z., Zhao, C., Zhang, Q., Haung, M., and Ma, X.: Statistical analysis of properties and parameterization of effective radius of warm cloud in Beijing area, Atmos. Res., 93, 888–896, 2009.

971 Devenish, B.J., Bartello, P., Brenguier, J.L., Collins, L.R., Grabowski, W.W., IJzermans,
 972 R.H.A., Malinowski, S.P., Reeks, M.W., Vassilicos, J.C., Wang, L.P. and Warhaft, Z., 2012.
 973 Droplet growth in warm turbulent clouds. Quarterly Journal of the Royal Meteorological Society,
 974 138(667), pp.1401-1429.

975 Doms, G, and U. Schattler, 2002: A description of the Nonhydrostatic Regional Model LM.
 976 Part 1: Dynamics and Numerics, Deutscher Wetterdienst, Geschäftsbereich Forschung und
 977 Entwicklung, Offenbach, Germany. (Available at <http://www.cosmo-model.org/>)

978 Fan J., and co-authors, 2018: Substantial convection and precipitation enhancements by
 979 ultrafine aerosol particles. Science, vol. 359, issue 6374, pp. 411-418.

980 Freud, E., D. Rosenfeld, M. O. Andreae, A.A Costa, and P. Artaxo, 2008:, Robust relations
 981 between CCN and the vertical evolution of cloud drop size distribution in deep convective clouds,
 982 Atmos. Chem. Phys., 8(6), 1661–1675, doi:10.5194/acp-8-1661-2008.

983 Freud, E., Rosenfeld, D., and Kulkarni, J. R., 2011: Resolving both entrainment-mixing and
 984 number of activated CCN in deep convective clouds, Atmos. Chem. Phys., 11, 12887-12900,
 985 doi:10.5194/acp-11-12887-2011.

986 Freud, E., and D. Rosenfeld, 2012: Linear relation between convective cloud drop number
 987 concentration and depth for rain initiation, J. Geophys. Res., 117, D02207,
 988 doi:10.1029/2011JD016457.

989 Garratt, J.R. 1992 The atmospheric boundary layer, Cambridge Atmospheric and Space
 990 Science Series, Cambridge University press, 319 pp.

991 Gerber, H., 2000: Structure of small cumulus clouds. Proc. 13th Intern. Conf, Clouds and
 992 Precip., Reno, NV, 14-18 Aug., 105-108.

Gerber, H, Frick G, Jensen J.B, and Hudson J.G., 2008: Entrainment, mixing, and microphysics in trade-wind cumulus. *J. Meteorol. Soc. Jpn.*, 86A. 87-106.

Ghan, S. J., Hayder Abdul-Razzak, A. Nenes, Yi Ming, Xiaohong Liu, M. Ovchinnikov, Ben Shipway, N. Meskhidze, Jun Xu, and X. Shi, 2011: Droplet nucleation: Physically-based parameterizations and comparative evaluation. *J. Adv. Model. Earth Syst.*, Vol. 3, M10001, 33 pp. DOI:10.1029/2011MS000074.

Grabowski, W.W. and G.C. Abade, 2017: Broadening of Cloud Droplet Spectra through Eddy Hopping: Turbulent Adiabatic Parcel Simulations. *J. Atmos. Sci.*, 74, 1485–1493, <https://doi.org/10.1175/JAS-D-17-0043.1>.

Heiblum R. H., O. Altaratz, I. Koren, G. Feingold, A. B. Kostinski, A. P. Khain, M. Ovchinnikov, E. Fredj, G. Dagan, L. Pinto, R. Yaish, Q. Chen, 2016a: Characterization of cumulus cloud fields using trajectories in the center of gravity versus water mass phase space: 1. Cloud tracking and phase space description, *J. Geophys. Res. Atmos.*, 121, 6336–6355, doi:10.1002/2015JD024193.

Heiblum R. H., O. Altaratz, I. Koren, G. Feingold, A. B. Kostinski, A. P. Khain, M. Ovchinnikov, E. Fredj, G. Dagan, L. Pinto, R. Yaish, Q. Chen, 2016b: Characterization of cumulus cloud fields using trajectories in the center of gravity versus water mass phase space: 2. Aerosol effects on warm convective clouds, *J. Geophys. Res. Atmos.*, 121, 6356–6373, doi:10.1002/2015JD024193.

Heus T., and H. J. J. Jonker, 2008: Subsiding Shells around Shallow Cumulus Clouds. *J. Atmos. Sci.*, 65, 1003-1018.

Hoffmann, F., Y. Noh, and S. Raasch, 2017: The Route to Raindrop Formation in a Shallow Cumulus Cloud Simulated by a Lagrangian Cloud Model. *J. Atmos. Sci.*, 74, 2125–2142, <https://doi.org/10.1175/JAS-D-16-0220.1>.

Holland, J. Z. and Rasmusson, E. M., 1973: Measurements of the atmospheric mass, energy, and momentum budgets over a 500-kilometer square of tropical ocean. *Mon. Wea. Rev.*, 101, 44–55.

Jaenicke, R. 1988: 9.3.1 Physical properties, in *Physical and Chemical Properties of the Air*, edited by G. Fischer, pp. 405-420, Springer, Berlin, doi:10.1007/10333390_72.

Jiang, H. and G. Feingold, 2006: The effect of aerosol on warm convective clouds: Aerosol-cloud-surface flux feedbacks in a new coupled large eddy model, *J. Geophys. Res.*, 111, D01202, doi: 10.1029/2005JD006138.

Jiang, H., H. Xue, A. Teller, G. Feingold, and Z. Levin, 2006: Aerosol effects on the lifetime of shallow cumulus, *Geophys. Res. Lett.*, 33, L14806, doi:10.1029/2006GL026024.

Jiang, H., G. Feingold, H. H. Jonsson, M.-L. Lu, P. Y. Chuang, R. C. Flagan, and J. H. Seinfeld (2008), Statistical comparison of properties of simulated and observed cumulus clouds in the vicinity of Houston during the Gulf of Mexico Atmospheric Composition and Climate Study (GoMACCS), *J. Geophys. Res.*, 113, D13205, doi:10.1029/2007JD009304.

Katzwinkel, J., H. Siebert, T. Heus and R. A. Shaw, 2014: Measurements of turbulent mixing and subsiding shells in trade wind cumuli. *Jas.* 71, 2810-2822.

Kaufman, Y. J., Koren, I., Remer, L. A., Rosenfeld, D., and Rudich, Y., 2005: The effect of smoke, dust, and pollution aerosol on shallow cloud development over the Atlantic Ocean, *Proceedings of the National Academy of Sciences of the United States of America*, 102, 11207-11212, 10.1073/pnas.0505191102.

1037 Khain, A. P., M. Ovchinnikov, M. Pinsky, A. Pokrovsky, and H. Krugliak, 2000: Notes on
1038 the state-of-the-art numerical modeling of cloud microphysics, *Atmos. Res.* 55, 159-224.

1039 Khain, A. P., A. Pokrovsky, M. Pinsky, A. Seifert, and V. Philips, 2004: Simulation of effects
1040 of atmospheric aerosols on deep turbulent convective clouds by using a spectral microphysics
1041 mixed-phase cumulus cloud model. Part I: Model description and possible applications. *J. Atmos.*
1042 *Sci.*, 61, 2963–2982.

1043 Khain, A. P. (2009), Notes on state-of-the-art investigations of aerosol effects on precipitation:
1044 a critical review, *Environ. Res. Lett.* 4 (2009) 015004 (20pp) doi:10.1088/1748-9326/4/1/015004.

1045 Khain, A. P., B. Lynn and J. Dudhia, 2010: Aerosol effects on intensity of landfalling
1046 hurricanes as seen from simulations with WRF model with spectral bin microphysics, *J. Atmos.*
1047 *Sci.* , 67, 365-384

1048 Khain, A., T. V. Prabha, N. Benmoshe, G. Pandithurai, and M. Ovchinnikov, 2013: The
1049 mechanism of first raindrops formation in deep convective clouds, *J. Geophys. Res. Atmos.*, 118,
1050 9123–9140, doi:10.1002/jgrd.50641

1051 Khain A.P., K. D. Beheng, A. Heymsfield, A. Korolev, S.O. Krichak, Z. Levin, M. Pinsky,
1052 V. Phillips, T. Prabhakaran, A. Teller, S.C. van den Heever, J.-I. Yano, 2015: Representation of
1053 microphysical processes in cloud-resolving models: spectral (bin) microphysics vs. bulk
1054 parameterization. *Review of Geophysics*, 53, Issue 2, 247–322.

1055 Khairoutdinov M. F. and Y. L. Kogan, 1999: A large eddy simulation model with explicit
1056 microphysics: validation against aircraft observations of a stratocumulus-topped boundary layer.
1057 *Jas.* 56, 2115-2131.

1058 Khairoutdinov M. and Y. Kogan, 2000: A New Cloud Physics Parameterization in a Large-
1059 Eddy Simulation Model of Marine Stratocumulus. *J. Atmos. Sci.* 128, 229-243.

1060 Khairoutdinov, M. F., and D. A. Randall (2003), Cloud resolving modeling of the ARM
1061 summer 1997 IOP: Model formulation, results, uncertainties, and sensitivities, *J. Atmos. Sci.*,
1062 60(4), 607–625, doi:10.1175/1520-0469.

1063 Khvorostyanov, V.I. and J.A. Curry, 1999: Toward the Theory of Stochastic Condensation in
1064 Clouds. Part I: A General Kinetic Equation. *J. Atmos. Sci.*, 56, 3985–
1065 3996, <https://doi.org/10.1175/1520-0469>.

1066 Kogan, Z. N. and Y. L. Kogan, 2001: Parameterization of drop effective radius for drizzling
1067 marine stratocumulus. *J. Geophys. Res.*, 106, 9757-9764.

1068 Kogan, Y. 2013: A cumulus cloud microphysics parametrization for cloud-resolving models.
1069 *Jas.* 70, 1423-1436.

1070 Koren, I., Y. J. Kaufman, D. Rosenfeld, L. A. Remer, and Y. Rudich, 2005: Aerosol
1071 invigoration and restructuring of Atlantic convective clouds, *Geophys. Res. Lett.*, 32, L14828.
1072 10.1029/2005gl023187

1073 Koren, I., Dagan, G. & Altaratz, O. 2014: From aerosol-limited to invigoration of warm
1074 convective clouds. *Science* 344, 1143–1146.

1075 Koren, I., Altaratz, O. & Dagan, G., 2015: Aerosol effect on the mobility of cloud droplets.
1076 *Environmental Research Letters* 10, 104011.

1077 Korn, G. A. and Korn, T. M., *Mathematical Handbook for Scientists and Engineers, 2nd*
1078 *Edition*, Dover Publications, New York, 2000.

1079 Kumar, B., S. Bera, T. V. Prabha, and W. W. Grabowski, 2017: Cloud-edge mixing: Direct
1080 numerical simulation and observations in Indian Monsoon clouds, *J. Adv. Model. Earth Syst.*,
1081 9, doi:10.1002/2016MS000731.

1082 Lehmann, K., H. Siebert, and R. A. Shaw, 2009: Homogeneous and inhomogeneous mixing
1083 in cumulus clouds: dependence on local turbulence structure. *J. Atmos. Sci.*, 66, 3641–3659.

1084 Levin, Z., and W.R. Cotton, 2009: Aerosol Pollution Impact on Precipitation. A Scientific
1085 Review . Springer, 386 p.

1086 Liu, Y., and P. H. Daum, 2000: Spectral dispersion of cloud droplet size distributions and the
1087 parameterization of cloud droplet effective radius, *Geophys. Res. Lett.*, 27, 1903–1906,
1088 doi:10.1029/1999GL011011.

1089 Long, A. 1974: Solution to the droplet collection equation for polynomial kernels, *J. Atmos.*
1090 *Sci.* , 31, 1040-1052.

1091 Lu, M.-L., G. Feingold, H. H. Jonsson, P. Y. Chuang, H. Gates, R. C. Flagan, and J. H.
1092 Seinfeld, 2008: Aerosol-cloud relationships in continental shallow cumulus, *J. Geophys. Res.*, 113,
1093 D15201, doi:10.1029/2007JD009354.

1094 Lu, C., Y. Liu, S. Niu, and S. Endo, 2014: Scale dependence of entrainment-mixing
1095 mechanisms in cumulus clouds, *J. Geophys. Res. Atmos.*, 119, 13,877–13,890,
1096 doi:10.1002/2014JD022265.

1097 Magaritz-Ronen L., M. Pinsky and A. Khain, 2014: Effects of turbulent mixing on the
1098 structure and macroscopic properties of stratocumulus clouds demonstrated by a Lagrangian
1099 trajectory model. *J. Atmos. Sci.* 71, 1843-1862.

1100 Magaritz-Ronen L., M. Pinsky, and A. Khain, 2016a: Drizzle formation in stratocumulus
1101 clouds: effects of turbulent mixing. *Atmos. Chem. Phys.*, 16, 1849–1862.

1102 Magaritz-Ronen, L., A. Khain, and M. Pinsky, 2016b: About the horizontal variability of
1103 effective radius in stratocumulus clouds, *J. Geophys. Res. Atmos.*, 121, 9640–9660,
1104 doi:10.1002/2016JD024977.

1105 Matheou, G., Chung, D., Nuijens, L., Stevens, B., & Teixeira, J.,2011: On the fidelity of
1106 large-eddy simulation of shallow precipitating cumulus convection. *Monthly Weather Review*,
1107 139(9), pp- 2918-2939.

1108 Martin, G. M., D. W. Johnson, and A. Spice, 1994: The measurement and parameterization
1109 of effective radius of droplets in warm stratocumulus clouds, *J. Atmos. Sci.*, 51, 1823-1842.

1110 Milbrandt J. A. and M. K. Yau, 2005: A multimoment bulk microphysics parameterization.
1111 Part I: Analysis of the role of the spectral shape parameter. *J. Atmos. Sci.*, 62, 3051-3064.

1112 Milbrandt J. A, and R. McTaggart-Cowan, 2010: Sedimentation-induced errors in bulk
1113 microphysics schemes. *J. Atmos. Sci.*, 67, 3931–3948.

1114 Nakajima, T., and M. D. King (1990), Determination of the optical Thickness and Effective
1115 Particle radius of clouds from reflected solar radiation measurment. Part 1: Theory, *J. Atmos. Sci.*,
1116 47, 1878–1893.

1117 Neggers R. A. J., H. J. J. Jonker, P. Siebesma, 2003: Size statistics of cumulus cloud
1118 populations in Large-Eddy simulations, *J. Atmos. Sci.*, 60, 1060-1074.

1119 Norris, J. R., Low cloud type over the ocean from surface observations. Part II: Geographical
1120 and seasonal variations, 1998: *Journal of climate*, 11(3), 383-403.

1121 Nuijens, L., B. Medeiros, I. Sandu, and M. Ahlgrimm (2015), The behavior of trade-wind
1122 cloudiness in observations and models: The major cloud components and their variability, *J. Adv.*
1123 *Model. Earth Syst.*, 7, 600–616, doi:10.1002/2014MS000390.

1124 Paluch, I. R., and D. Baumgardner, 1989: Entrainment and fine-scale mixing in a continental
1125 convective cloud. *J. Atmos. Sci.* 46, 261-273.

1126 Paluch, I. R., and C.A. Knight, 1984: Mixing and the evolution of cloud droplet size spectra
1127 in a vigorous continental cumulus. *J. Atmos. Sci.*, 41, 1801-1815.

Paluch, I. R., 1986: Mixing and the cloud droplet size spectrum: Generalizations from the CCOPE data, *J. Atmos. Sci.*, 43, 1984-1993.

Pinsky, M., Khain, A. P., and M. Shapiro (2001), Collision efficiency of drops in a wide range of Reynolds numbers: Effects of pressure on spectrum evolution, *J. Atmos. Sci.* 58, 742-764.

Pinsky, M. and A. P. Khain, 2002: Effects of in-cloud nucleation and turbulence on droplet spectrum formation in cumulus clouds. *Quart. J. Roy. Meteorol. Soc.*, 128, 1–33.

Pinsky M., A. Khain, H. Krugliak, 2008: Collisions of cloud droplets in a turbulent flow. Part 5: application of detailed tables of turbulent collision rate enhancement to simulation of droplet spectra evolution. *J. Atmos. Sci.*, 65, 357-374.

Pinsky, M., A. Khain, I. Mazin, and A. Korolev, 2012: Analytical estimation of droplet concentration at cloud base. *J. Geophys. Res.* 117, D18211, doi:10.1029/2012JD017753.

Pinsky, M., I.P. Mazin, A. Korolev, and A. Khain, 2013: Supersaturation and diffusional drop growth in liquid clouds, *J. Atmos. Sci.*, 70, 2778-2793.

Pinsky, M., I. Mazin, A. Korolev and A. Khain, 2014: Supersaturation and diffusional droplet growth in liquid clouds: Polydisperse spectra. *J. Geophys Res.* 2014, 119, 12872-12887.

Pinsky, M., Khain, A., Korolev, A., and Magaritz-Ronen, L., 2016a: Theoretical investigation of mixing in warm clouds – Part 2: Homogeneous mixing, *Atmos. Chem. Phys.*, 16, 9255–9272, 2016, www.atmos-chem-phys.net/16/9255/2016/ doi:10.5194/acp-16-9255-2016.

Pinsky, M., Khain, A., and Korolev, A. 2016b: Theoretical analysis of mixing in liquid clouds – Part 3: Inhomogeneous mixing, *Atmos. Chem. Phys.*, 16, 9273–9297, 2016; www.atmos-chem-phys.net/16/9273/2016/doi:10.5194/acp-16-9273-2016.

1149 Pinsky, M. and A. Khain, 2018a: Theoretical Analysis of the Entrainment–Mixing
 1150 Process at Cloud Boundaries. Part I: Droplet Size Distributions and Humidity within the
 1151 Interface Zone. *J. Atmos. Sci.*, 75, 2049–2064, <https://doi.org/10.1175/JAS-D-17-0308.1>
 1152 Pinsky, M. and A. Khain, 2018b: Theoretical analysis of mixing in liquid clouds –
 1153 Part IV: DSD evolution and mixing diagrams, *Atmos. Chem. Phys.*, 18, 3659–3676,
 1154 <https://doi.org/10.5194/acp-18-3659-2018>.
 1155 Pontikis, C. A. (1996), Parameterization of the droplet effective radius of warm layer clouds,
 1156 *Geophys. Res. Lett.*, 23(19), 2629–2632.
 1157 Prabha, T. V., A. Khain, R. S. Maheshkumar, G. Pandithurai, J. R. Kulkarni, M. Konwar, and
 1158 B. N. Goswami, 2011: Microphysics of premonsoon and monsoon clouds as seen from in situ
 1159 measurements during the Cloud Aerosol Interaction and Precipitation Enhancement Experiment
 1160 (CAIPEEX), *J. Atmos. Sci.*, 68, 1882–1901.
 1161 Raga, G. B., J. B. Jensen, and M. B. Baker, 1990: Characteristics of cumulus band clouds off
 1162 the coast of Hawaii, *J. Atmos. Sci.*, 47, 338–355, doi:10.1175/1520-
 1163 0469(1990)047<0338:COCBCO>2.0.CO;2.
 1164
 1165 Reid J. S., P. V. Hobbs, A. L. Rangno, and 876 D. A. Hegg, 1999: Relationships between
 1166 cloud droplet effective radius, liquid water content, and droplet concentration for warm clouds in
 1167 Brazil embedded in biomass smoke. *J. Geophys. Res.*, 104, 6145–6153.
 1168
 1169 Reisin, T., Z. Levin, and S. Tzivion, 1996: Rain production in convective clouds as simulated
 1170 in an axisymmetric model with detailed microphysics. Part 1: Description of the model. *J. Atmos.*
 1171 *Sci.*, 53, 497–519.

1172 Riechelmann, T., Noh, Y. and Raasch, S., 2012. A new method for large-eddy simulations of
 1173 clouds with Lagrangian droplets including the effects of turbulent collision. *New Journal of*
 1174 *Physics*, 14(6), p.065008.

1175 Rosenfeld, D., and I. M. Lensky, 1998: Satellite-Based Insights into Precipitation Formation
 1176 Processes in Continental and Maritime Convective Clouds, *Bull. Am. Meteorol. Soc.*, 79, 2457–
 1177 2476, doi:10.1175/1520-0477.

1178 Rosenfeld D., U. Lohmann, G.B. Raga, C.D. O’Dowd, M. Kulmala, S. Fuzzi, A. Reissell,
 1179 M.O. Andreae (2008), Flood or Drought: How Do Aerosols Affect Precipitation? *Science*, 321,
 1180 1309-1313.

1181 Rosenfeld, D., B. Fischman, Y. Zheng, T. Goren, and D. Giguzin, 2014: Combined satellite
 1182 and radar retrievals of drop concentration and CCN at convective cloud base, *Geophys. Res. Lett.*,
 1183 41(9), 3259–3265, doi:10.1002/2014GL059453.

1184 Rosenfeld D., Y. Zheng, E. Hashimshoni, M. L. Pöhlker, A. Jefferson, C. Pöhlker, X. Yu, Y.
 1185 Zhu, G. Liu, Z. Yue, B. Fischman, Z. Li, D. Giguzin, T. Goren, P. Artaxoi, H. M. J. Barbosai, U.
 1186 Pöschl, and Meinrat O. Andreae, 2016: Satellite retrieval of cloud condensation nuclei
 1187 concentrations by using clouds as CCN chambers. *Proceedings of the National Academy of*
 1188 *Sciences*, doi:10.1073/pnas.1514044113.

1189 Savijarvi H., A. Arola and P. Raisanen, 1997: Short-wave optical properties of precipitating
 1190 water clouds. *Q. J. R. Meteorol. SOC.* (1997), 123, pp. 883-899

1191 Savijarvi H., A. and P. Raisanen, 1998: Long-wave optical properties of water clouds and
 1192 rain. *Tellus* (1998), 50A, 1–11

1193 Schmeissner, T., R.A. Shaw, J. Ditas, F. Stratmann, M. Wendisch and H. Siebert, 2015:
 1194 Turbulent mixing in shallow trade wind cumuli: dependence on cloud life cycle. *J. Atmos. Sci.* 72,
 1195 1447-1465.

1196 Segal Y. and A. P. Khain (2006), Dependence of droplet concentration on aerosol conditions
 1197 in different cloud types: application to droplet concentration parameterization of aerosol
 1198 conditions, *J. Geophys. Res.* Vol. 111, D15204, doi:10.1029/2005JD006561.

1199 Seifert, A., Nuijens, L. and Stevens, B., 2010: Turbulence effects on warm-rain
 1200 autoconversion in precipitating shallow convection. *Quart.J.R. Meteorol. Soc.*, 136: 1753–1762.
 1201 doi:10.1002/qj.684.

1202 Seifert, A., and T. Heus (2013), Large-eddy simulation of organized precipitating trade wind
 1203 cumulus clouds, *Atmos. Chem. Phys.*, 13, 5631–5645.

1204 Seifert, A., T. Heus, R. Pincus and B. Stevens, 2015: Large-eddy simulation of the transient
 1205 and near-equilibrium behavior of precipitating shallow convection, *J. Adv. Model. Earth Syst.*, 7,
 1206 1918–1937, doi:10.1002/2015SMS0000489.

1207 Seiki, T. and Nakajima, T. 2014: Aerosol effects of the condensation process on a convective
 1208 cloud simulation. *Journal of the Atmospheric Sciences* 71, 833–853.

1209 Shaw, R. A., 2003: Particle-turbulence interactions in atmospheric clouds, *Annu. Rev. Fluid*
 1210 *Mech.*, 35, 183-227.

1211 Shima, S.I., Kusano, K., Kawano, A., Sugiyama, T. and Kawahara, S., 2009: The super-
 1212 droplet method for the numerical simulation of clouds and precipitation: A particle-based and
 1213 probabilistic microphysics model coupled with a non-hydrostatic model. *Quarterly Journal of the*
 1214 *Royal Meteorological Society*, 135(642), pp.1307-1320.

1215 Siebesma, A.P., Bretherton, C.S., Brown, A., Chlond, A., Cuxart, J., Duynkerke, P.G.,

1216 Jiang, H., Khairoutdinov, M., Lewellen, D., Moeng, C.H. and Sanchez, E., 2003. A large eddy
 1217 simulation intercomparison study of shallow cumulus convection. *Journal of the Atmospheric*
 1218 *Sciences*, 60(10), pp.1201-1219.

1219 Small, J. D., Chuang, P. Y., Feingold, G., & Jiang, H., 2009: Can aerosol decrease cloud
 1220 lifetime? *Geophysical Research Letters*, 36(16).

1221 Squires, P., 1958: The microstructure and colloidal stability of warm clouds, *Tellus*, 10, 262-
 1222 271,.

1223 Squires, P., and Twomey, S.: The relation between cloud droplet spectra and the spectrum of
 1224 cloud nuclei, *Geophysical Monograph Series*, 5, 211-219, 1960.

1225 Stephens, G. L., Li, J., Wild, M., Clayson, C. A., Loeb, N., Kato, S., L'Ecuyer, T., Stackhouse,
 1226 P. W., Lebsock, M. and Andrews, T. 2012: An update on Earth's energy balance in light of the
 1227 latest global observations, *Nat. Geosci.*, 5(10), 691–696, doi:10.1038/ngeo1580.

1228 Steppeler J, Doms G, Schattler U, Bitzer HW, Gassmann A, Damrath U, Gregoric G. 2003:
 1229 Meso-gamma scale forecasts using the nonhydrostatic model LM. *Meteorology and Atmospheric*
 1230 *Physics* 82: 75-96.

1231 Stevens, B., C. Moeng, and P. Sullivan, 1999: Large-eddy simulations-of radiatively driven
 1232 convection: Sensitivities to the representation of small scales, *J. Atmos. Sci.*, 56(23), 3963–3984.

1233 Stevens, B., and Seifert, A., 2008: Understanding macrophysical outcomes of microphysical
 1234 choices in simulations of shallow cumulus convection. *Journal of the Meteorological Society of*
 1235 *Japan*, 86, pp. 143-162.

1236 Szczodrak M., P. H. Austin and P. B. Krummel, 2001: Variability of Optical Depth and
 1237 Effective Radius in Marine Stratocumulus Clouds. *J. Atmos. Sci.* 58, 2912-2926.

1238 Tao W.-K., Jen-Ping Chen, Zhanqing Li, Chien Wang, Chidong Zhang (2012), Impact of
 1239 Aerosols on Convective Clouds and Precipitation. *Reviews of Geophysics*. Volume 50, Issue 2,
 1240 June 2012 DOI: 10.1029/2011RG000369.

1241 Tas, E., Teller, A., Altaratz, O., Axisa, D., Bruintjes, R., Levin, Z., and Koren, I.: The relative
 1242 dispersion of cloud droplets: its robustness with respect to key cloud properties, *Atmos. Chem.*
 1243 *Phys.*, 15, 2009-2017, doi:10.5194/acp-15-2009-2015, 2015.

1244 Tas, E., I. Koren, and O. Altaratz: On the sensitivity of droplet size relative dispersion to warm
 1245 cumulus cloud evolution, *Geophys. Res. Lett.*, 39, L13807, doi:10.1029/2012GL052157, 2012.

1246 Trenberth, K. 2011: Changes in precipitation with climate change, *Clim. Res.*, 47(1), 123–
 1247 138, doi:10.3354/cr00953.

1248 Twomey S., 1974: Pollution and the planetary albedo. *Atmos. Envir.*, 8, 1251-1256.

1249 Twomey, S., 1977: The Influence of Pollution on the Shortwave Albedo of Clouds, *J. Atmos.*
 1250 *Sci.*, 34(7), 1149–1152, doi:10.1175/1520-0469

1251 Tzivion, S., G. Feingold, and Z. Levin, 1987: An efficient numerical solution to the stochastic
 1252 collection equation. *J. Atmos. Sci.*, 44, 3139-3149.

1253 Yuan, T., Remer, L. A., and Yu, H., 2011: Microphysical, macrophysical and radiative
 1254 signatures of volcanic aerosols in trade wind cumulus observed by the A-Train, *Atmospheric*
 1255 *Chemistry and Physics*, 11, 7119-7132, 10.5194/acp-11-7119-2011.

1256 VanZanten, M. C. M. C., B. Stevens, G. Vali, and D. H. Lenschow (2005), Observations of
 1257 drizzle in nocturnal marine stratocumulus, *J. Atmos. Sci.*, 62(12), 88–106 ST – Observations of
 1258 drizzle in nocturnal , doi:10.1175/JAS3611.1.

1259 Wang L. P., and Grabowski W., 2009: The role of air turbulence in warm rain initiation.
 1260 *Atmos. Sci., Let.* 10, 1-8.

Warner, J., and Twomey, S. 1967: The production of cloud nuclei by cane fires and the effect on cloud droplet concentration, *Journal of the atmospheric Sciences*, 24, 704-706,.

Wendish M. and J._L. Brenguier, 2013: *Airborne Measurements for Environmental Research: Methods and Instruments*, see chapter 5: *In-situ measurements of Cloud and Precipitation particles*. Wiley, pp. 304.

Wiscombe W.J., R.M. Welch and W.D. Hall, 1984: the effects of very large drops on cloud absorption. Part 1: Parcel models. *J. Atmos. Sci.*, 41, 1336-1355.

Wong M. and M. Ovchinnikov, 2017: Parameterization of subgrid-scale hydrometeor transport in deep convection. *J. Atmos. Sci.*, 74, 1293-1309.

Xue H., and G. Feingold, 2006: Large-Eddy simulation of trade wind cumuli: investigation of aerosol indirect effects. *J. Atmos. Sci.*, 63, 1605-1622.

Zhang, S., H. Xue, and G. Feingold, 2011: Vertical profiles of droplet effective radius in shallow convective clouds, *Atmos. Chem. Phys.*, 11(10), 4633–4644, doi:10.5194/acp-11-4633-2011.

Zhang Y., S. A. Klein, J. Fan, A. S. Chandra, P. Kollias, S. Xie and S. Tang, 2017: Large-eddy simulations of shallow cumulus over land: a composite case based on ARM long-term observations at Its Southern Great Plains site, *JAS*. 74, 3229-3251.

Zheng, Y., and D. Rosenfeld (2015), Linear relation between convective cloud base height and updrafts and application to satellite retrievals, *Geophys. Res. Lett.*, 42, 6485–6491, doi:10.1002/2015GL064809.

Tables

Table 1. List of simulations. Notations: “total CF” – time averaged total cloud fraction, “STD of total CF” – standard deviation of total CF, “ $\langle N_d \rangle$ ” – time and space averaged N_d , “ $\langle CWC \rangle$ max” – maximum (over height) value of the mean profile of CWC, “ $\langle r_e \rangle$ max” – maximum (over height) value of the mean profile of r_e .

Name of experiment	Height of inversion (m)	Aerosol concentration (cm^{-3})	Main results				
			total CF (%)	STD of total CF (%)	$\langle N_d \rangle$ (cm^{-3})	$\langle CWC \rangle$ max (gm^{-3})	$\langle r_e \rangle$ max (μm)
E5000L	1000	5000	20.1	1.8	403	0.52	7.7
E5000M	1500	5000	17.9	1.0	371	0.54	8.2
E5000H	2000	5000	19.7	1.6	372	0.47	8.4
E3000L	1000	3000	20.5	1.6	248	0.58	9.4
E3000M	1500	3000	18.7	1.7	222	0.52	9.8
E3000H	2000	3000	20.4	1.7	221	0.47	10.2
E2000L	1000	2000	20.8	1.1	164	0.58	10.7
E2000M	1500	2000	18.8	1.1	149	0.51	11.3

E2000H	2000	2000	20.6	1.5	148	0.48	12
E1000L	1000	1000	21.9	1.0	81	0.55	13.6
E1000M	1500	1000	19.4	1.3	82	0.49	14.9
E1000H	2000	1000	21.7	1.6	83	0.42	15.5
E500L	1000	500	24.2	1.8	47	0.43	16.7
E500M	1500	500	21.5	1.3	49	0.37	18.2
E500H	2000	500	23.1	1.8	48	0.32	18.3

Figure captions

Figure 1. Initial vertical profiles of temperature (solid lines) and dew point (dashed) used in simulations: low inversion at 1000 m (black), high inversion at 2000m (blue), middle inversion at 1500m (red) (the original BOMEX profile). Green and cyan profiles denote sensitivity tests with decreased relative humidity (by 5% and 10%, respectively) with respect to high inversion profile.

Figure 2. Time evolution of the cloud fraction in simulations with 1500 m inversion base height for different CN concentrations.

Figure 3. A snapshot of (a) CWC, (b) N_d , and (c) r_e fields for E5000H experiment: inversion is at 2 km, the CN concentration is 5000 cm^{-3} , $t = 208 \text{ min}$. The impression of "noodle" shape clouds and not the usual "cotton balls" shape, are just due to the difference between the horizontal and vertical scales.

Figure 4. The vertical profiles of cloud water content $\overline{CWC}(z)$ averaged over all clouds (a), rain water content $\overline{RWC}(z)$ (b) droplet concentration $\overline{N_d}(z)$ (c) and effective radius $\overline{r_e}(z)$ (d), in different simulations. $\overline{CWC}(z)$, $\overline{N_d}(z)$ and $\overline{r_e}(z)$ are plotted for $CWC > 0.01 \text{ gm}^{-3}$. \overline{RWC} is plotted for $RWC > 0.01 \text{ gm}^{-3}$.

Figure 5. Vertical profiles of mean CF in the different simulations determined by total LWC (a) and by cloud droplets only (b).

Figure 6. Vertical profiles of "effective" optical depth in different simulations calculated using eq. (1) for cloud droplets (a) and rain drops (b). Thin dotted lines at optical depth lower than ~ 0.01 in (a) show the upper parts of cloud layers with contribution to the total optical depth is below than 5%.

Figure 7. Frequency by altitude diagrams of the CWC (left column) and RWC (right column) occurrence in the E500H, E2000H and E5000H simulations. The color scale shows the number of cloudy grid points with specific CWC or RWC plotted in logarithmic scale. Black lines show

maximum values of CWC that were found in cloud interior. Brown lines denote the modeled approximation to adiabatic LWC. Blue lines show the vertical profiles of cloud averaged values.

Figure 8. Height-droplet concentration occurrence (frequency) diagrams for the same simulations discussed in Fig. 7. The color reflects the number of cloudy grid points with specific N_d in logarithmic scale. Black lines show droplet concentration in cloud cores in points where CWC is maximal. Blue lines show the vertical profiles of cloud averaged values; brown lines show the modeled approximation to adiabatic values. The green dots show the $r_{e,ad} = 12\mu m$ level.

Figure 9. Scattering diagram r_v vs. r_e in obtained in simulations E500H, E2000H and E5000H. The color reflects the number of cloudy grid points with specific r_v and r_e in logarithmic scale. Black line denotes the linear fit. Black dashed lines show 1:1 relation.

Figure 10. The height- r_e scattering diagrams for simulations with different CN concentrations. Left, middle and right columns show the cases with low (base at 1000m), middle (base at 1500m) and high (base at 2000m) inversion, respectively. Notations: The color-scale reflects the number of cloudy grid points with specific r_e in logarithmic scale; black curves denote effective radii in clouds cores; purple curves denote the modeled approximation to adiabatic r_e profiles; blue curves denote profiles of horizontally averaged r_e ; black dashed lines denote the inversion base heights.

Figure 11. Vertical profiles of the cloud averaged effective radius calculated directly from LES (solid lines) and parameterized using Eqs. (5-7) (dashed lines). Each panel is plotted for different inversion base height: low, medium and high, respectively.

Figure 12. Profiles of cloud averaged droplet concentration obtained in LES (solid lines) and using expressions (8) and (9) (dashed lines). Each panel is plotted for different inversion base height: low, medium and high, respectively.

Figure 13. Vertical profiles of the cloud averaged CWC calculated directly from LES (solid lines) and approximation (11) (dashed lines) for different aerosol loadings and for different inversion levels: low (left), medium (middle) and high (right). Cyan solid and dashed lines indicate the profiles obtained using different options within the current parameterization in COSMO.

Figure 14. Vertical profiles of optical depth calculated by formula (1) using the approximation expressions (7) and (11) (dashed lines) and the average values calculated directly in LES (solid lines). Each panel corresponds to a certain inversion level: low (left), medium (middle) and high (right).

Figure 15. Comparison of mean effective radius profiles simulated using SAM with observations. Simulated mean r_e profiles: E5000H (black line), E2000H (blue solid line), E2000H-50 (blue dashed line), E500H (magenta). Blue empty squares show results of in-situ observations during GoMaCCS in polluted atmosphere (Jiang et al, 2008, Lu et al., 2008), black empty circles

(dissolving Cu) and black filled circles (developing Cu) show results of in-situ observations during CARRIBA (Schmeissner et al., 2015). Green filled squares show results reported by Gerber et al. (2008) obtained in flight RF12 during RICO. Brown-red-yellow color map shows r_e occurrence frequency from flight RF07 during RICO (Arabas et al., 2009). The extremely low values of r_e at heights around 1500m in the color map are likely related to dissipating cloud fragments.

Figure 16. Comparison of mean LWC profile simulated using SAM with observations. Red solid and dashed lines show results of E2000H and E2000H-50, respectively, using 0.01 gm^{-3} as threshold of minimum LWC. Green solid and dashed lines show results of E2000H and E2000H-50, respectively, but using 0.05 gm^{-3} as threshold of minimum LWC. Blue solid line shows the results of E2000L (threshold of 0.01 gm^{-3}). Black dotted line shows results of Warner (1955) taken from Gerber (2000). Black dashed line is calculated by averaging the LWC measured during SCMS (Gerber 2000); Black filled squares show results reported by Gerber (2008). Blue empty squares show results of in-situ measurements during GoMaCCS (Jiang et al, 2008). Cyan symbols denote values of cloud averaged LWC obtained during RICO at different aircrafts: crosses (Bac146), diamonds (C-130), squares (King Air). Combined values on 19 January 2005 are shown by cyan filled circles (Abel and Shipway, 2007).

Figure 17. PDF of 90th percentile of the adiabatic fraction within clouds in (a) CARRIBA measurements (Katzwinkel et al., 2014 fig. 3a therein) and in (b) E2000H simulation around height of 1500m. Similarly, PDF of 90th percentile of vertical velocity is presented for (c) measurements (Katzwinkel et al., 2014 fig. 3c therein) and (d) simulation. The measurements were performed

1405 around 100 m below cloud tops, with effective resolution of 20 cm. E2000H simulations results
1406 are presented for heights of 1380-1540 m.

1407

1408 Figure 18. Vertical profiles of averaged simulated (solid lines) and parametrized (dashed lines)
1409 effective radii. Blue: E2000H, green: E2000H-50, red: E2000H-RH1, black: E2000H-RH2.

1410

1411

1412

1413

1414

1415

1416

1417

1418

1419

1420 **Figures**

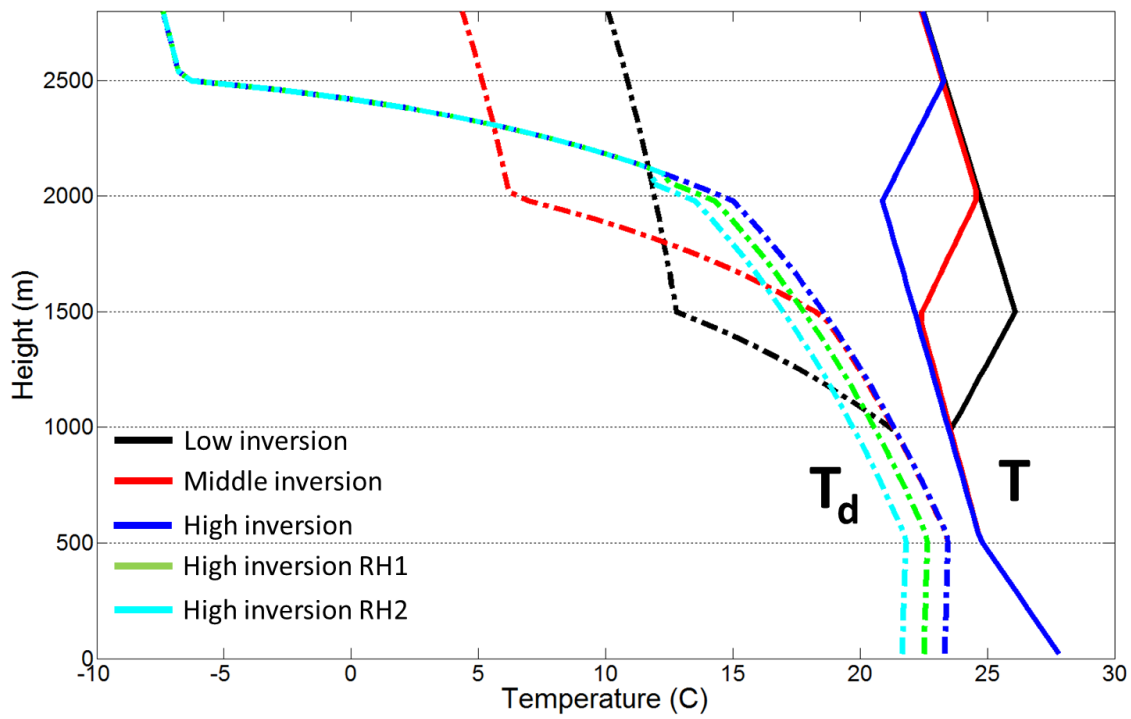


Figure 1. Initial vertical profiles of temperature (solid lines) and dew point (dashed) used in simulations: low inversion at 1000 m (black), high inversion at 2000m (blue), middle inversion at 1500m (red) (the original BOMEX profile). Green and cyan profiles denote sensitivity tests with decreased relative humidity (by 5% and 10%, respectively) with respect to high inversion profile.

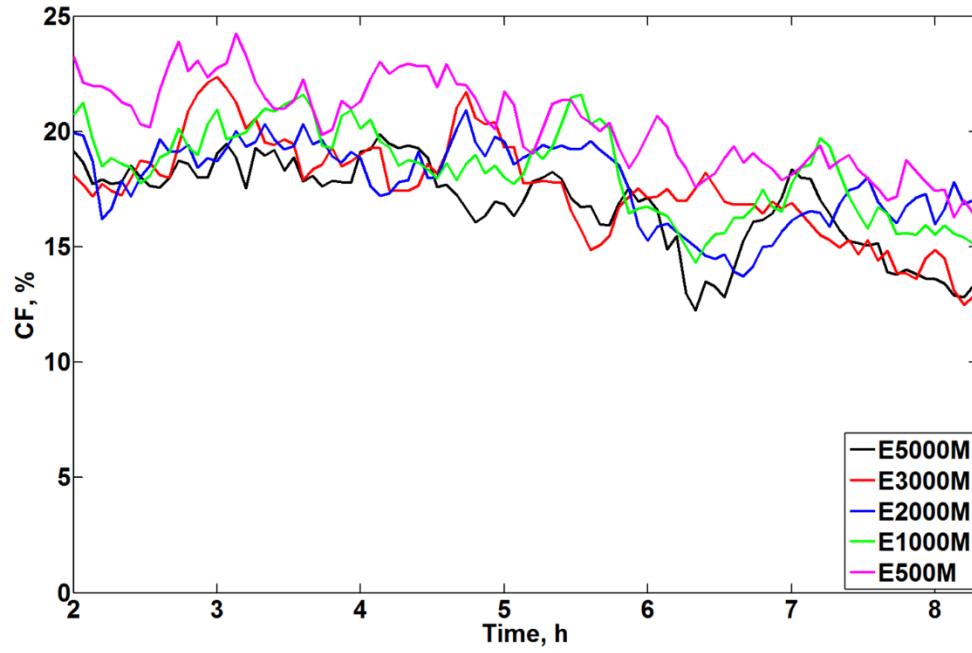


Figure 2. Time evolution of the cloud fraction in simulations with 1500 m inversion base height for different CN concentrations.

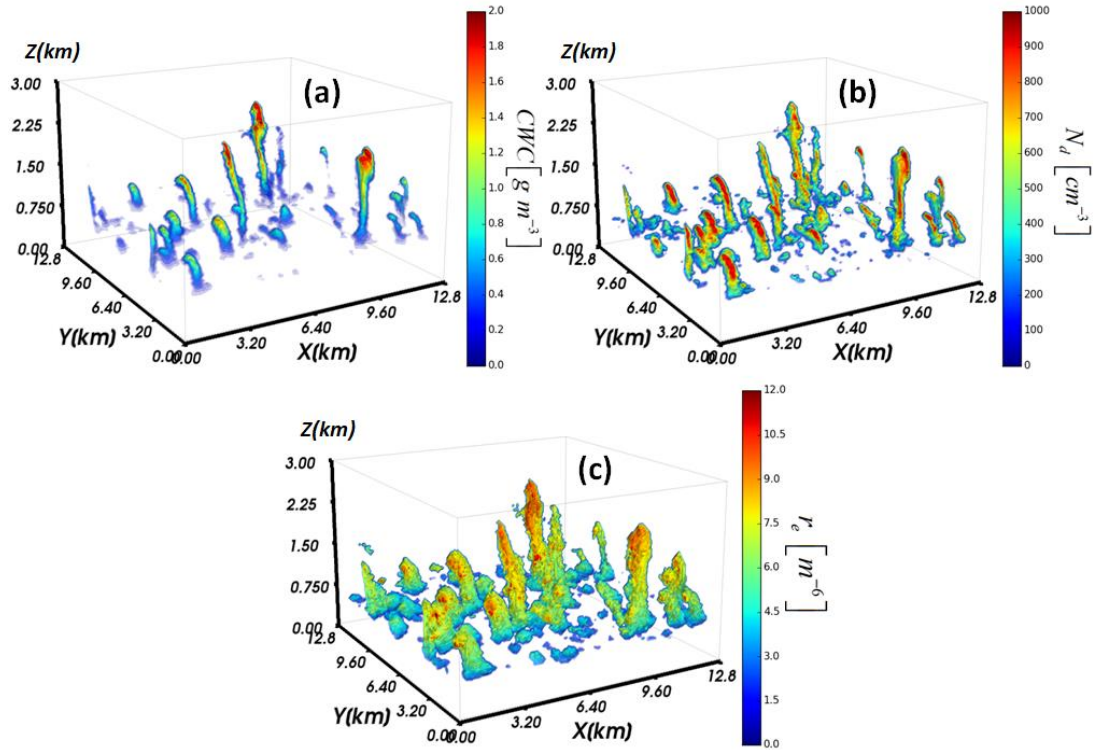


Figure 3. A snapshot of (a) CWC, (b) N_d , and (c) r_e fields for E5000H experiment: inversion is at 2 km, the CN concentration is 5000 cm^{-3} , $t = 208 \text{ min}$. The impression of "noodle" shape clouds and not the usual "cotton balls" shape, are just due to the difference between the horizontal and vertical scales.

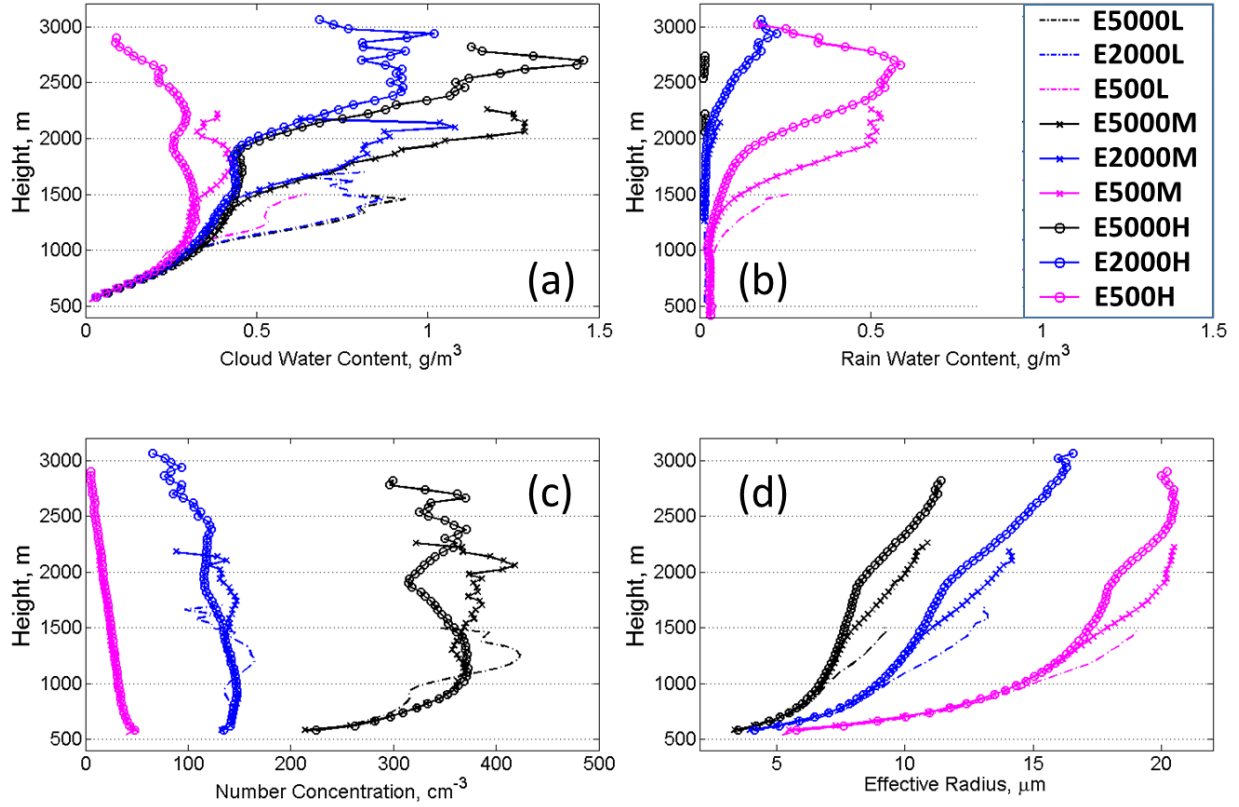


Figure 4. The vertical profiles of cloud water content $\overline{CWC}(z)$ averaged over all clouds (a), rain water content $\overline{RWC}(z)$ (b) droplet concentration $\overline{N_d}(z)$ (c) and effective radius $\overline{r_e}(z)$ (d), in different simulations. $\overline{CWC}(z)$, $\overline{N_d}(z)$ and $\overline{r_e}(z)$ are plotted for $CWC > 0.01 \text{ g/m}^3$. \overline{RWC} is plotted for $RWC > 0.01 \text{ g/m}^3$.

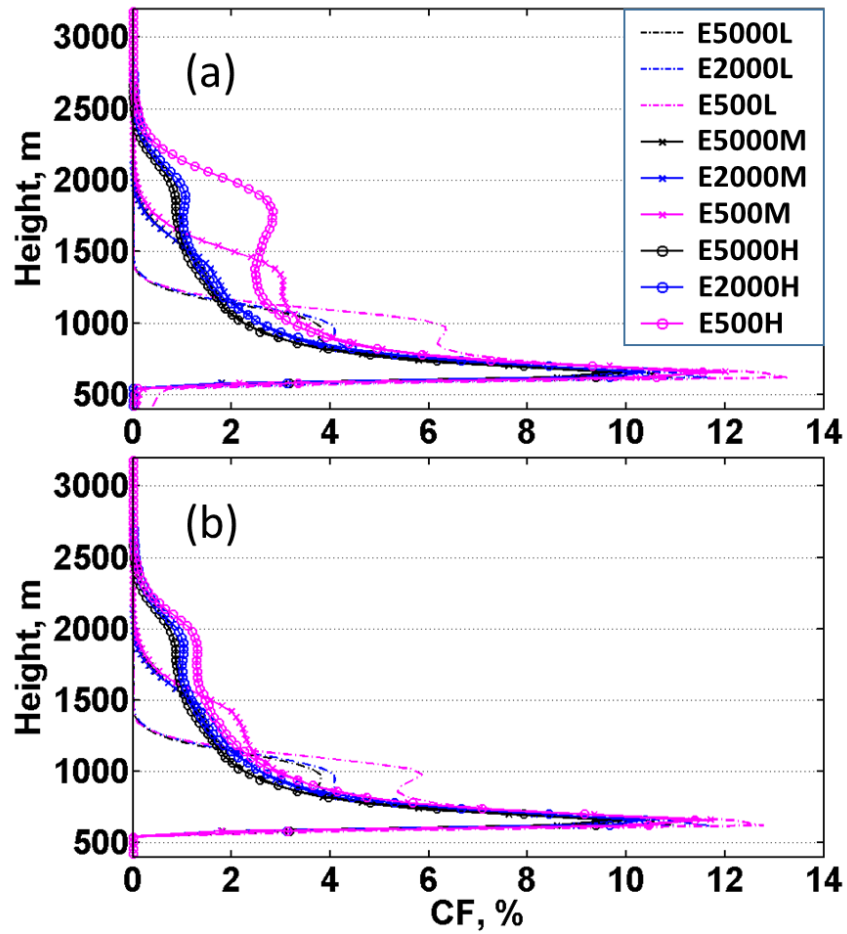


Figure 5. Vertical profiles of mean CF in the different simulations determined by total LWC (a) and by cloud droplets only (b).

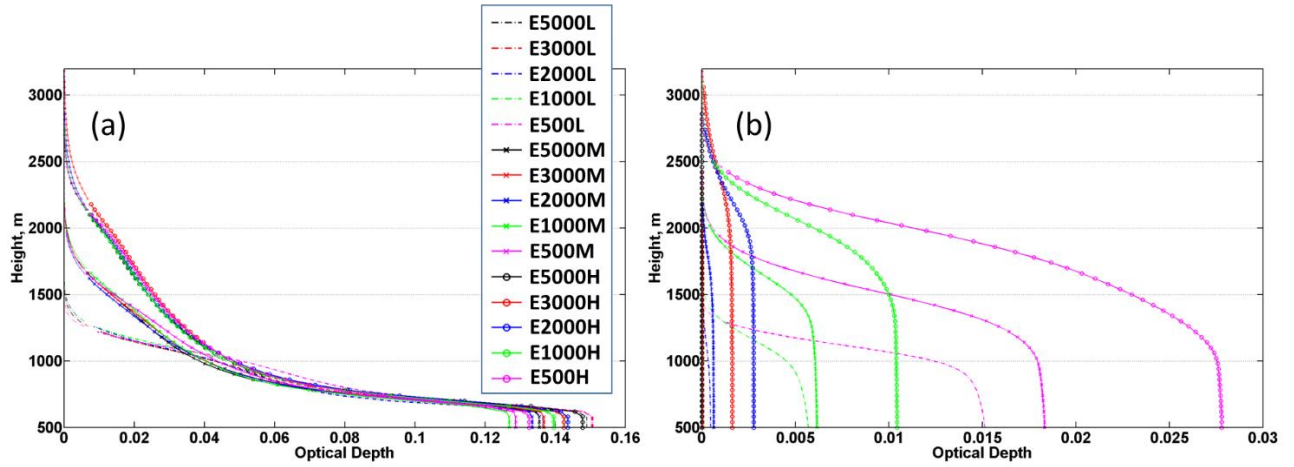


Figure 6. Vertical profiles of “effective” optical depth in different simulations calculated using eq. (1) for cloud droplets (a) and rain drops (b). Thin dotted lines at optical depth lower than ~ 0.01 in (a) show the upper parts of cloud layers with contribution to the total optical depth is below than 5%.

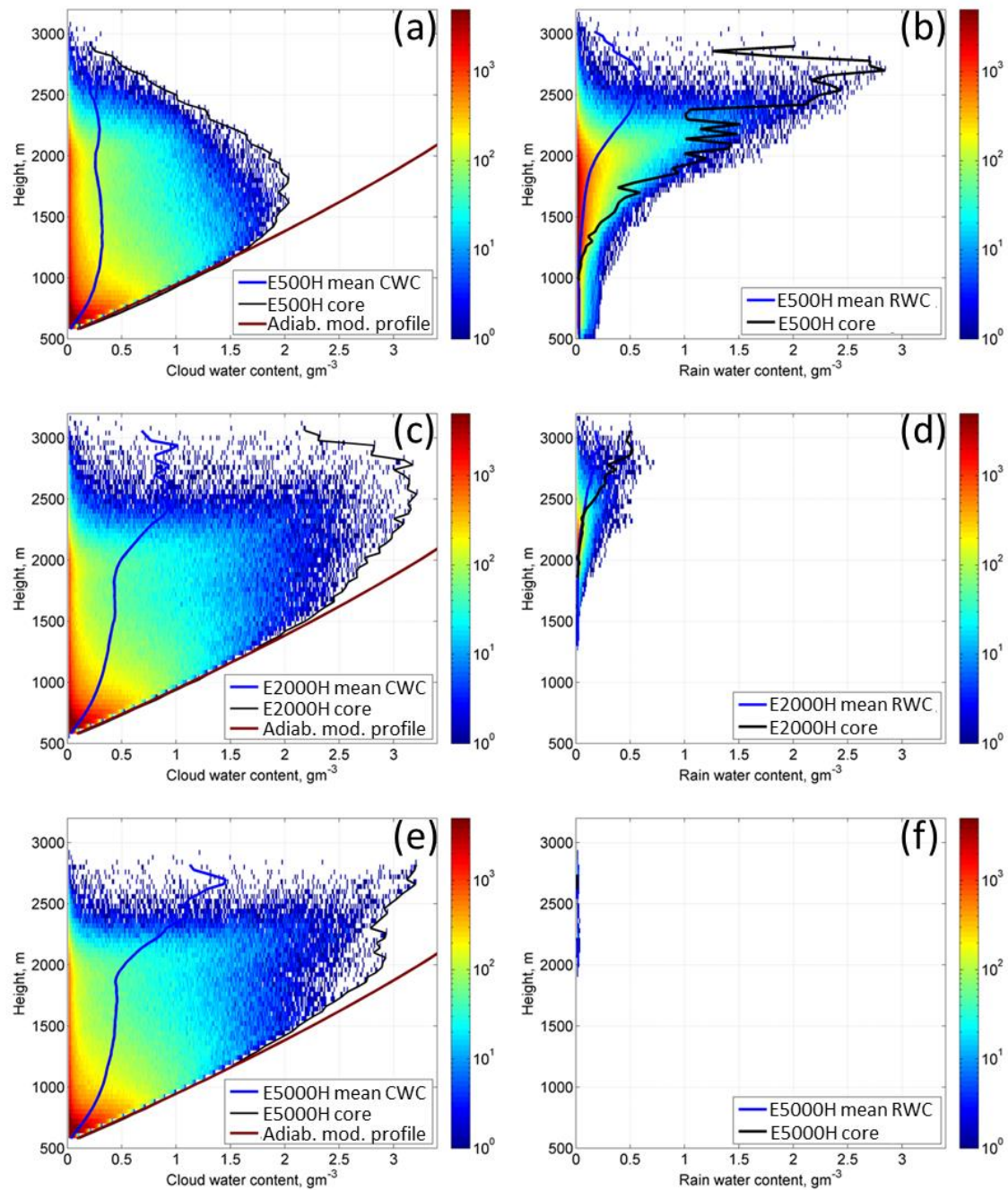


Figure 7. Frequency by altitude diagrams of the CWC (left column) and RWC (right column) occurrence in the E500H, E2000H and E5000H simulations. The color scale shows the number of cloudy grid points with specific CWC or RWC plotted in logarithmic scale. Black lines show maximum values of CWC that were found in cloud interior. Brown lines denote the modeled approximation to adiabatic LWC. Blue lines show the vertical profiles of cloud averaged values.

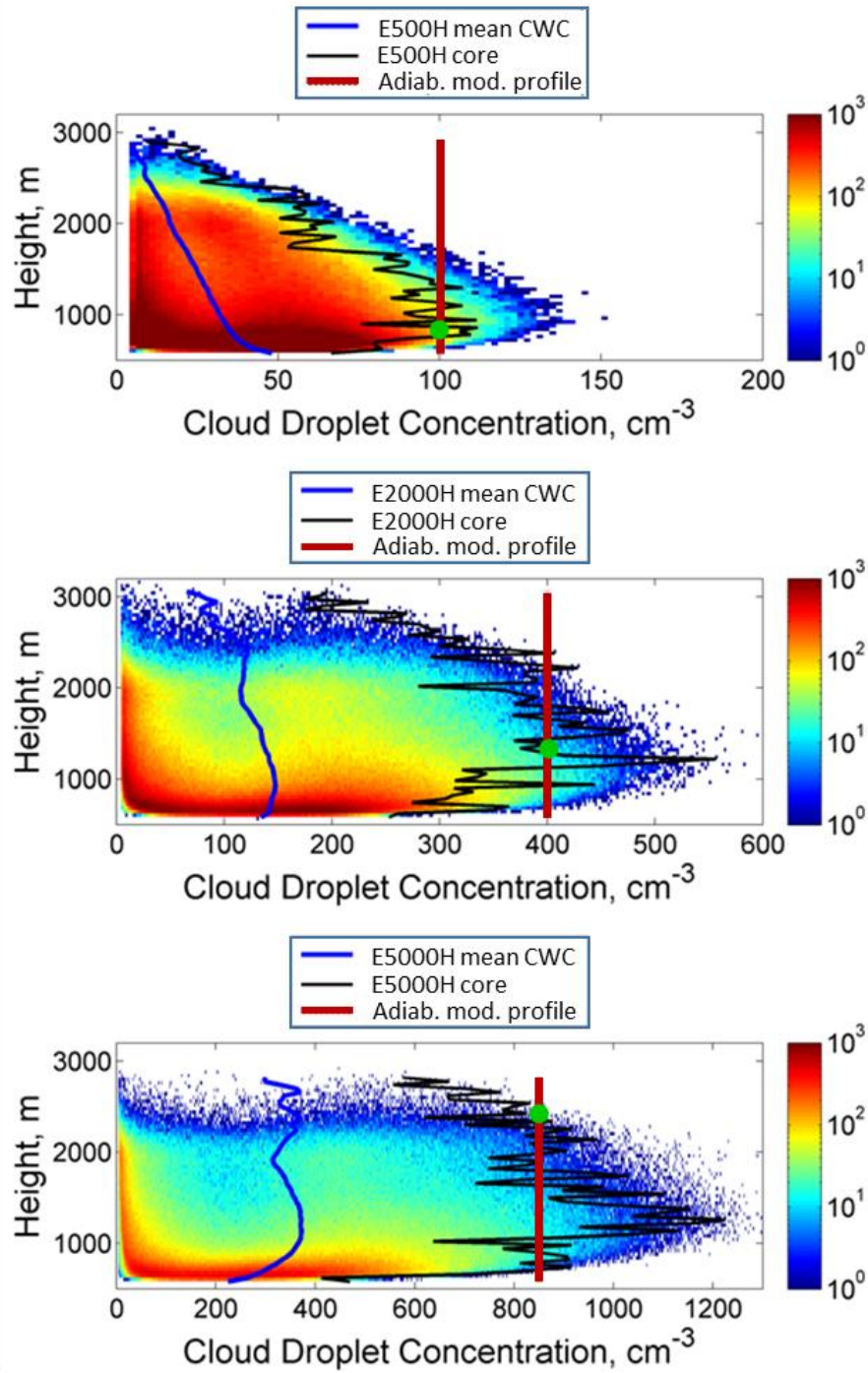
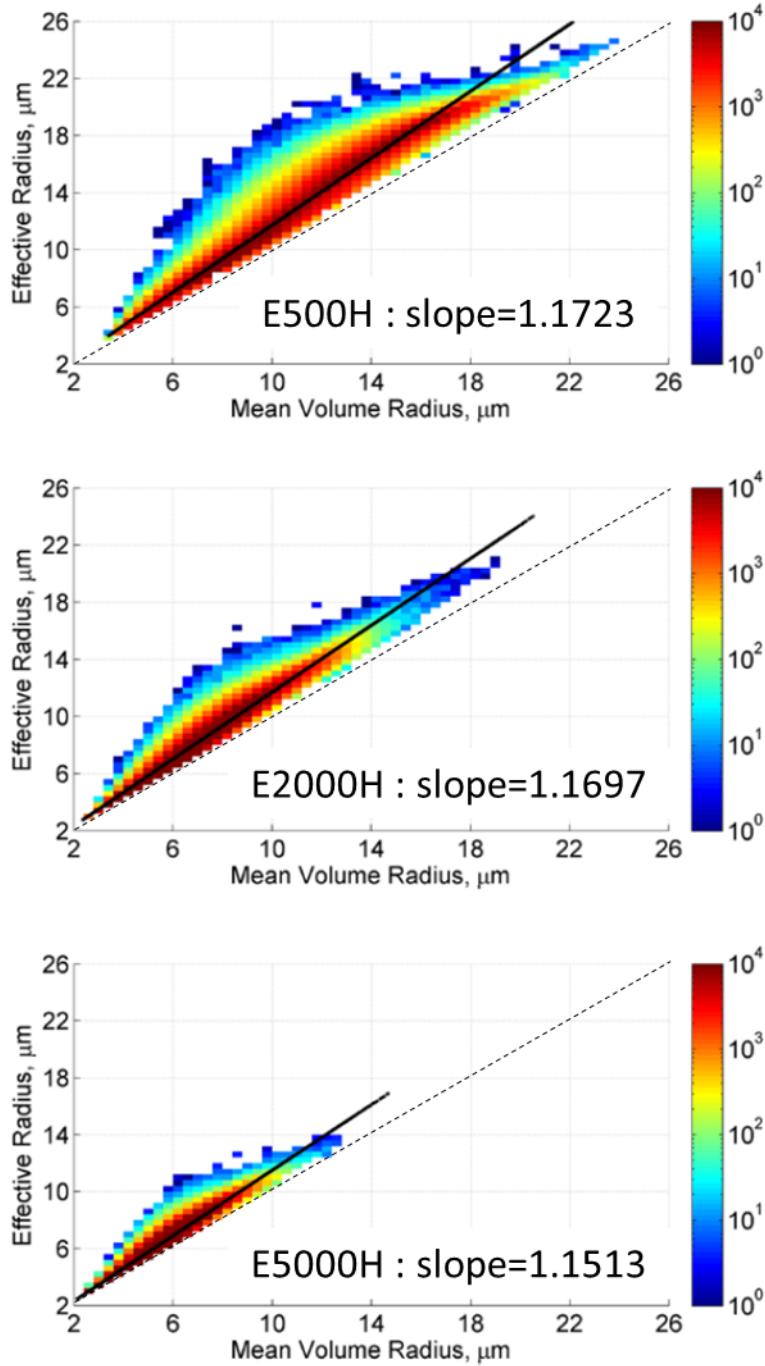


Figure 8. Height-droplet concentration occurrence (frequency) diagrams for the same simulations discussed in Fig. 7. The color reflects the number of cloudy grid points with specific N_d in logarithmic scale. Black lines show droplet concentration in cloud cores in points where CWC is maximal. Blue lines show the vertical profiles of cloud averaged values; brown lines show the modeled approximation to adiabatic values. The green dots show the $r_{e,ad} = 12 \mu m$ level.



1519

1520 Figure 9. Scattering diagram r_v vs. r_e in obtained in simulations E500H, E2000H and
 1521 E5000H. The color reflects the number of cloudy grid points with specific r_v and r_e in logarithmic
 1522 scale. Black line denotes the linear fit. Black dashed lines show 1:1 relation.

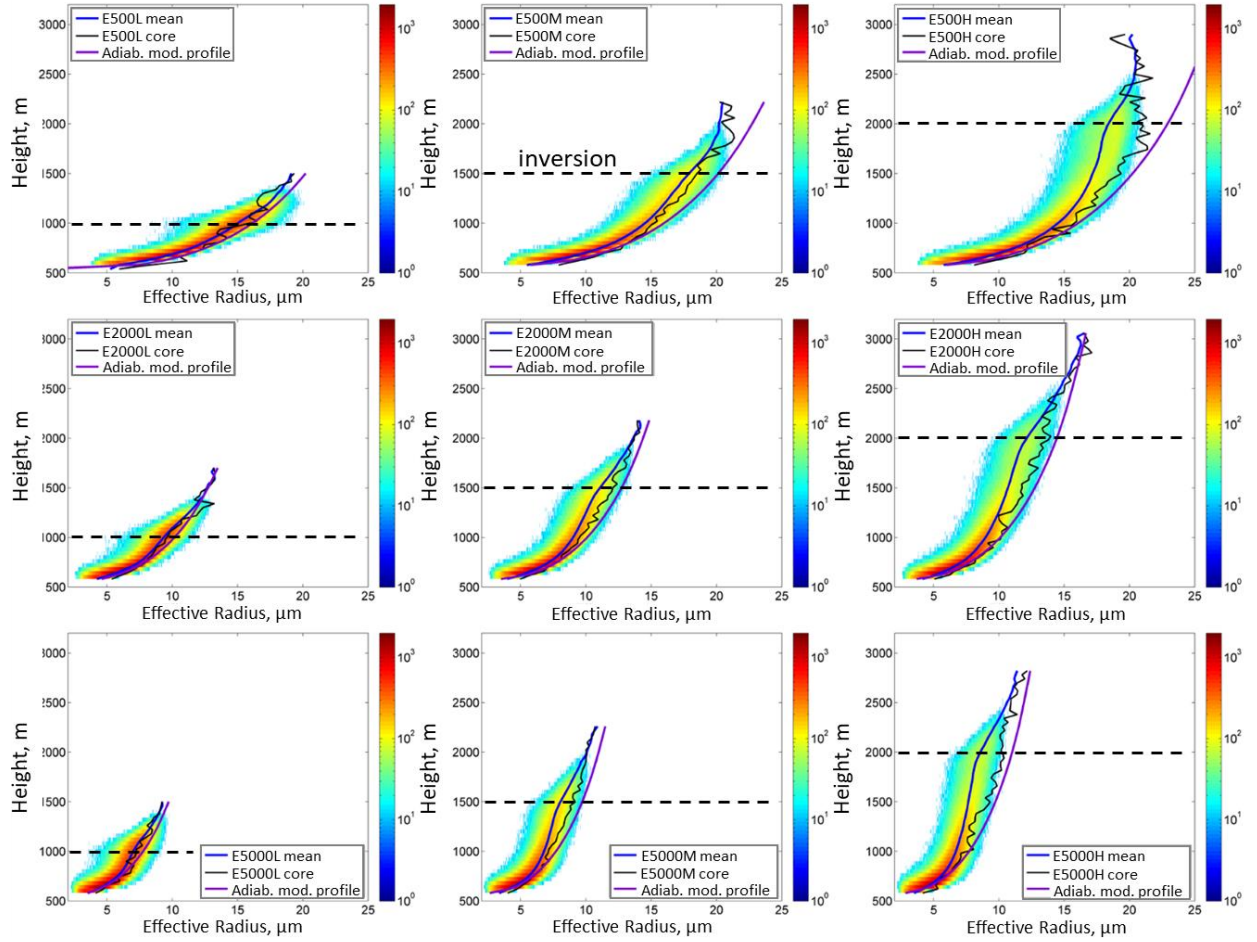


Figure 10. The height- r_e scattering diagrams for simulations with different CN concentrations. Left, middle and right columns show the cases with low (base at 1000m), middle (base at 1500m) and high (base at 2000m) inversion, respectively. Notations: The color-scale reflects the number of cloudy grid points with specific r_e in logarithmic scale; black curves denote effective radii in clouds cores; purple curves denote the modeled approximation to adiabatic r_e profiles; blue curves denote profiles of horizontally averaged r_e ; black dashed lines denote the inversion base heights.

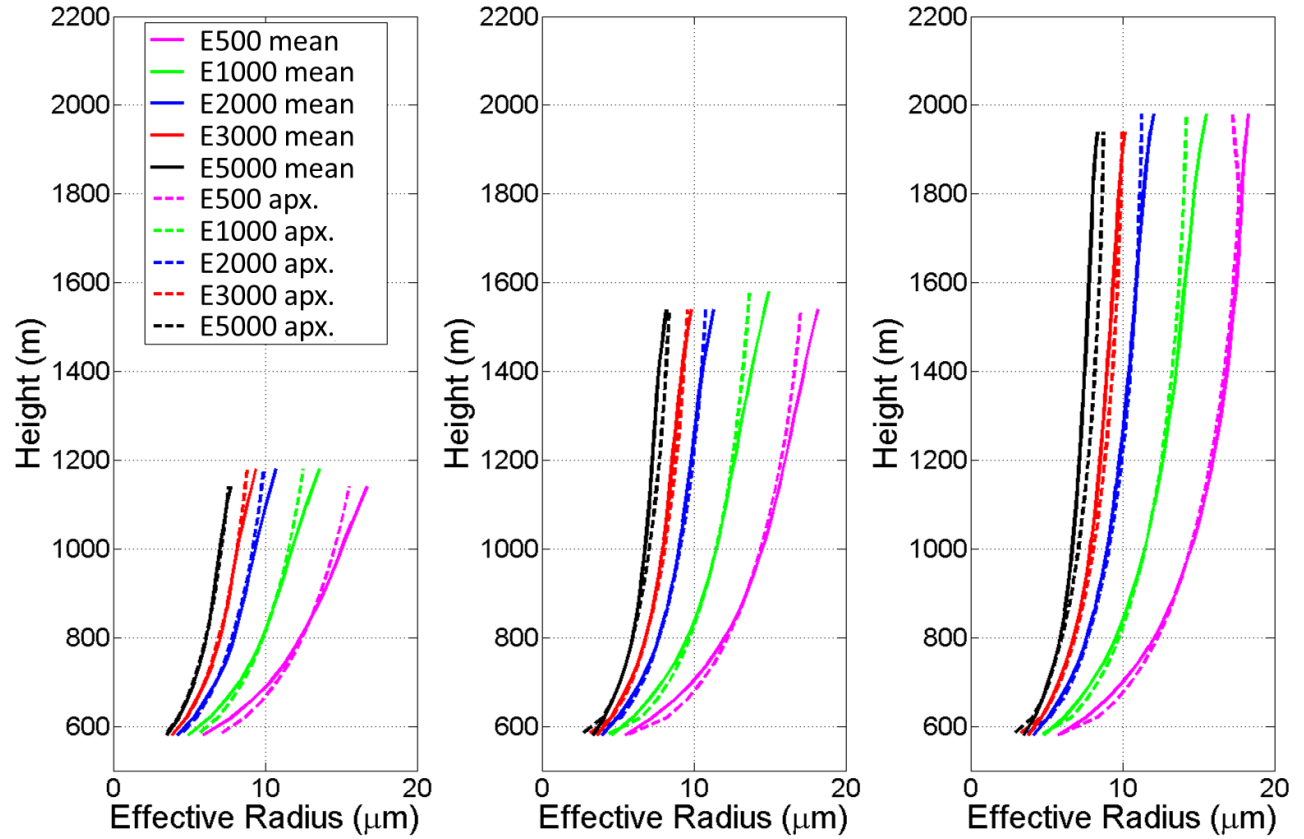


Figure 11. Vertical profiles of the cloud averaged effective radius calculated directly from LES (solid lines) and parameterized using Eqs. (5-7) (dashed lines). Each panel is plotted for different inversion base height: low, medium and high, respectively.

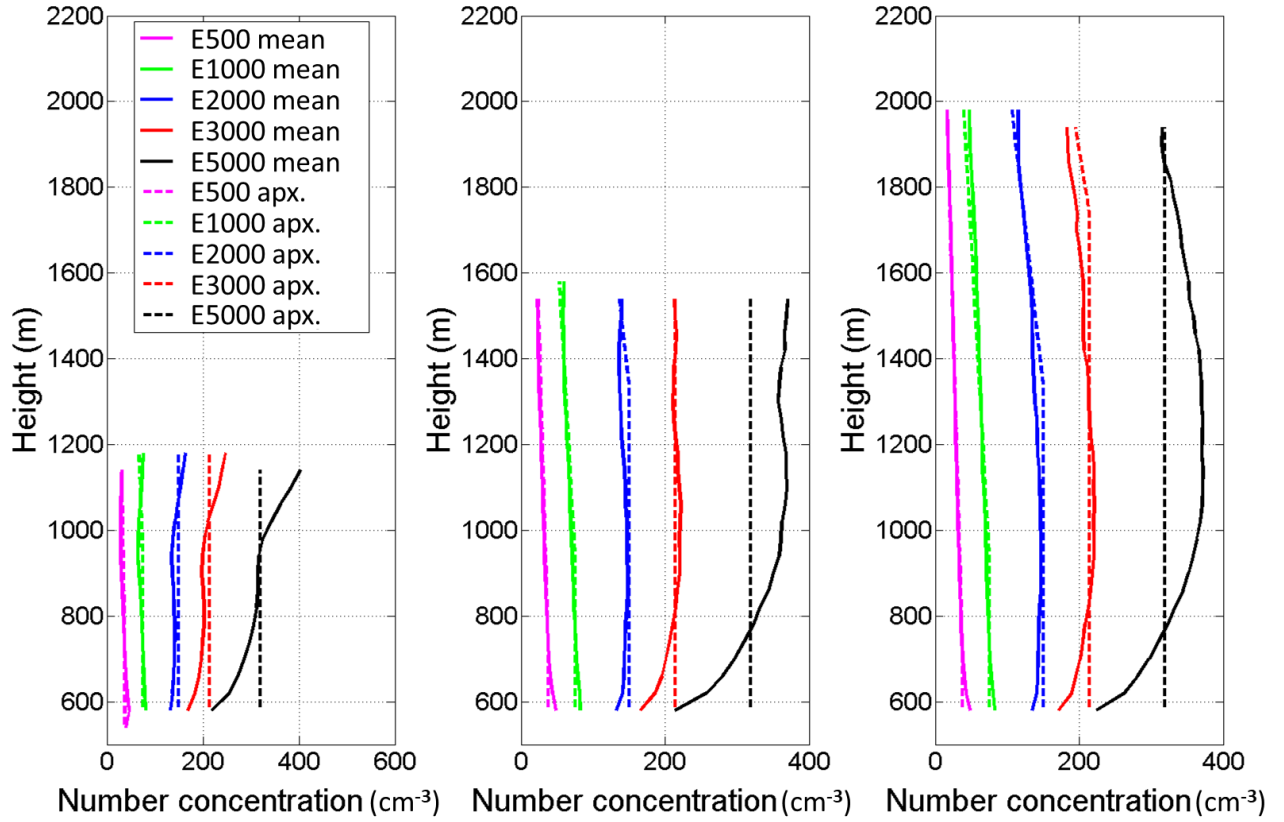


Figure 12. Profiles of cloud averaged droplet concentration obtained in LES (solid lines) and using expressions (8) and (9) (dashed lines). Each panel is plotted for different inversion base height: low, medium and high, respectively.

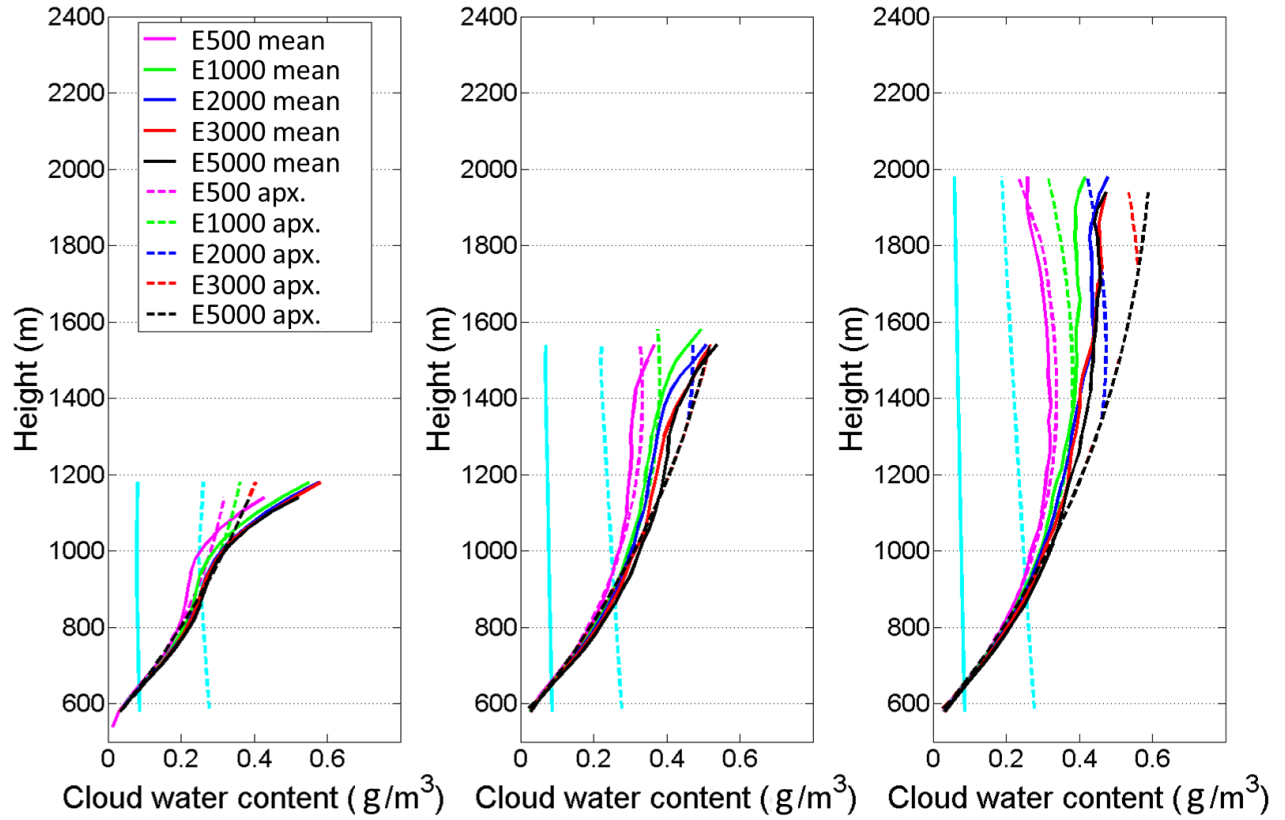


Figure 13. Vertical profiles of the cloud averaged CWC calculated directly from LES (solid lines) and approximation (11) (dashed lines) for different aerosol loadings and for different inversion levels: low (left), medium (middle) and high (right). Cyan solid and dashed lines indicate the profiles obtained using different options within the current parameterization in COSMO.

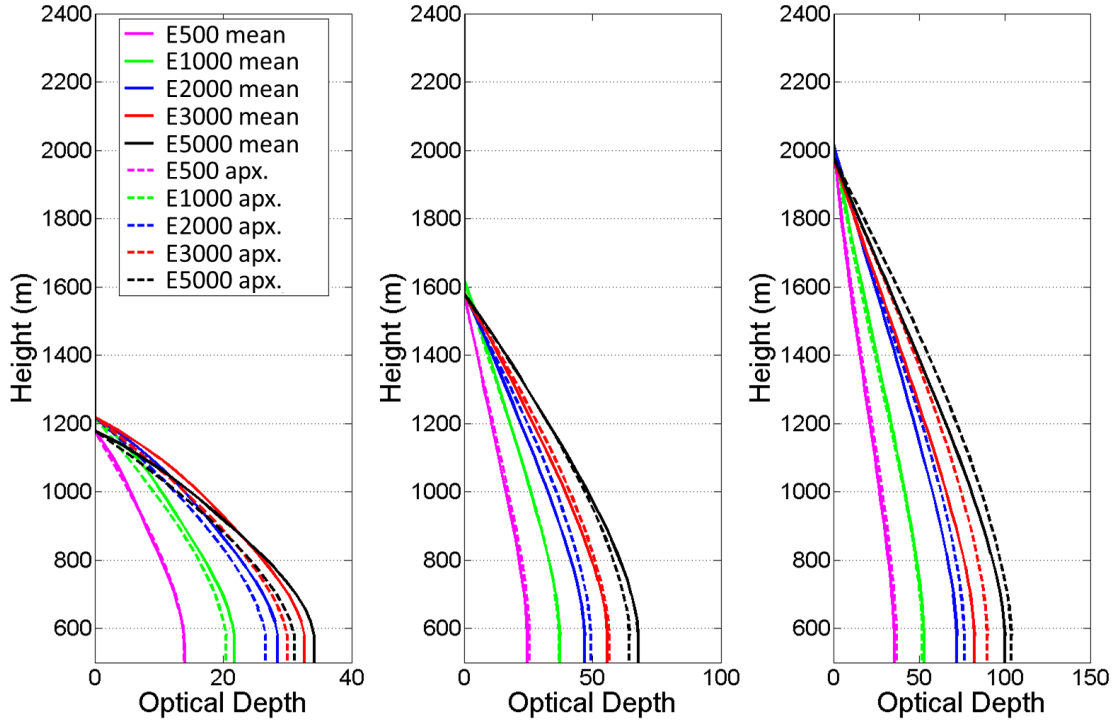


Figure 14. Vertical profiles of optical depth calculated by formula (1) using the approximation expressions (7) and (11) (dashed lines) and the average values calculated directly in LES (solid lines). Each panel corresponds to a certain inversion level: low (left), medium (middle) and high (right).

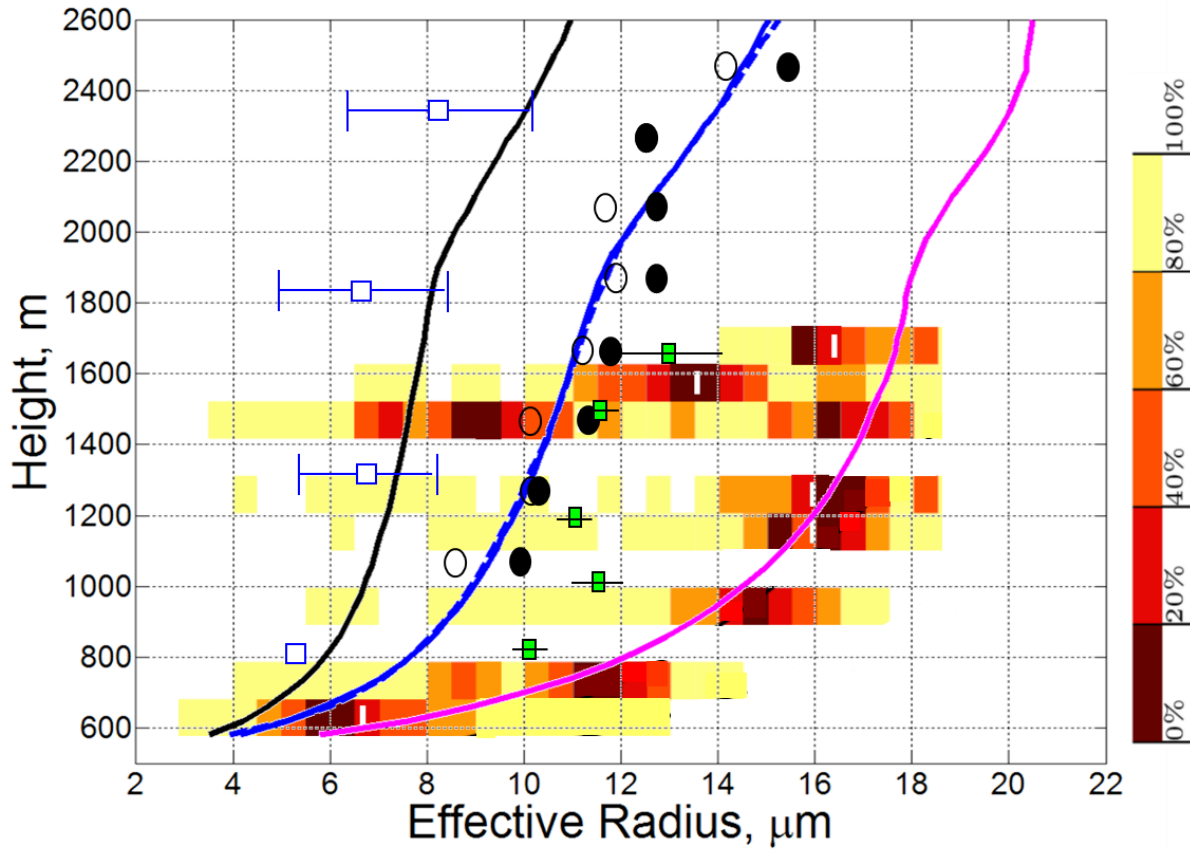


Figure 15. Comparison of mean effective radius profiles simulated using SAM with observations. Simulated mean r_e profiles: E5000H (black line), E2000H (blue solid line), E2000H-50 (blue dashed line), E500H (magenta). Blue empty squares show results of in-situ observations during GoMaCCS in polluted atmosphere (Jiang et al, 2008, Lu et al., 2008), black empty circles (dissolving Cu) and black filled circles (developing Cu) show results of in-situ observations during CARRIBA (Schmeissner et al., 2015). Green filled squares show results reported by Gerber et al. (2008) obtained in flight RF12 during RICO. Brown-red-yellow color map shows r_e occurrence frequency from flight RF07 during RICO (Arabas et al., 2009). The extremely low values of r_e at heights around 1500m in the color map are likely related to dissipating cloud fragments.

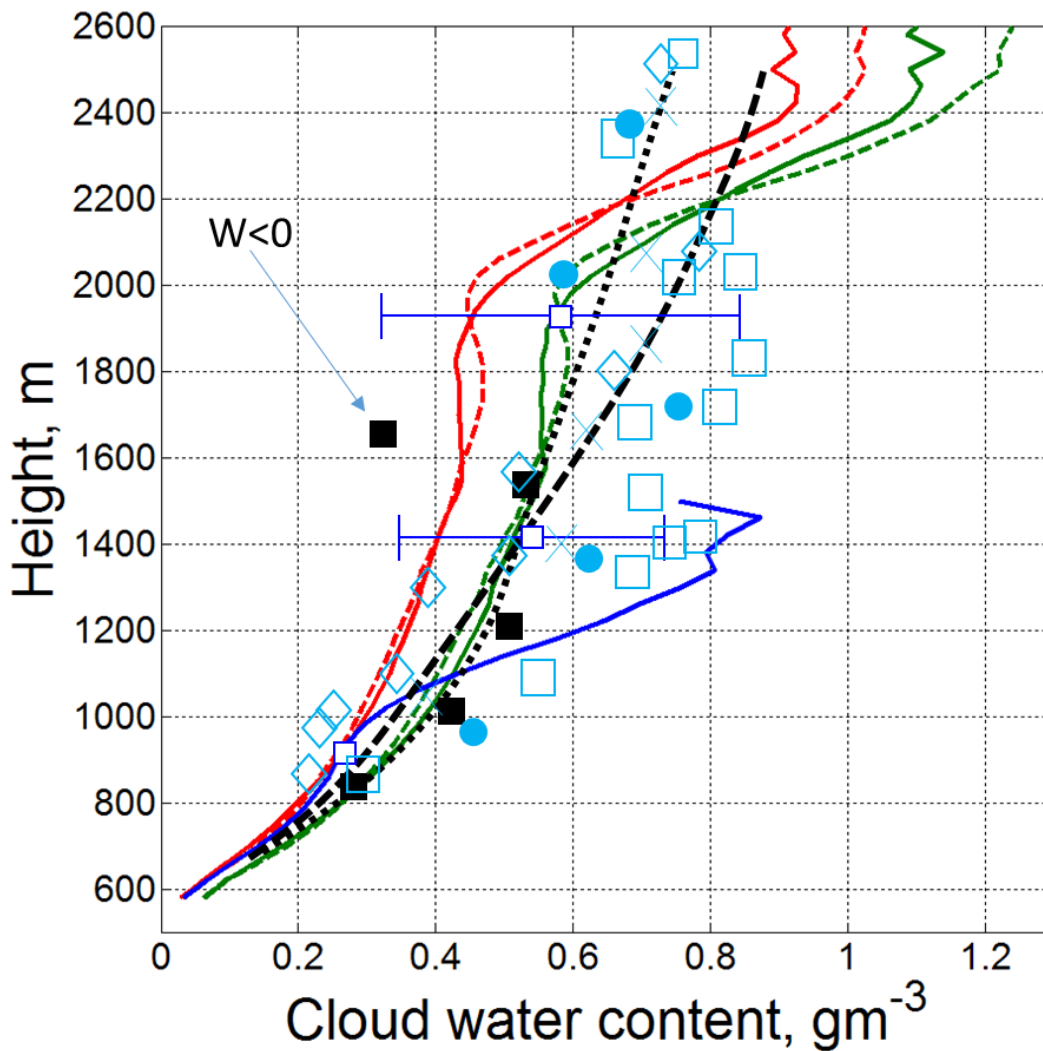


Figure 16. Comparison of mean LWC profile simulated using SAM with observations. Red solid and dashed lines show results of E2000H and E2000H-50, respectively, using 0.01 gm^{-3} as threshold of minimum LWC. Green solid and dashed lines show results of E2000H and E2000H-50, respectively, but using 0.05 gm^{-3} as threshold of minimum LWC. Blue solid line shows the results of E2000L (threshold of 0.01 gm^{-3}). Black dotted line shows results of Warner (1955) taken from Gerber (2000). Black dashed line is calculated by averaging the LWC measured during SCMS (Gerber 2000); Black filled squares show results reported by Gerber (2008). Blue empty squares show results of in-situ measurements during GoMaCCS (Jiang et al, 2008). Cyan symbols denote values of cloud averaged LWC obtained during RICO at different aircrafts: crosses (Bac146), diamonds (C-130), squares (King Air). Combined values on 19 January 2005 are shown by cyan filled circles (Abel and Shipway, 2007).

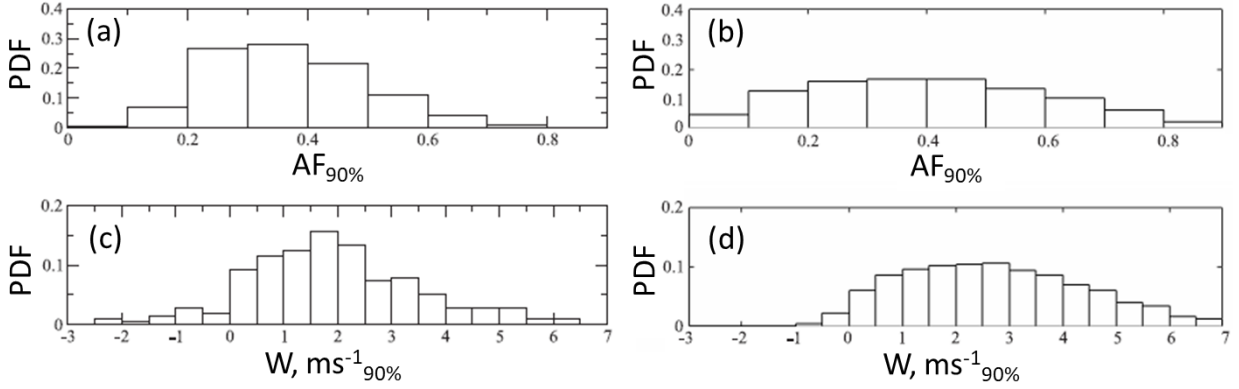


Figure 17. PDF of 90th percentile of the adiabatic fraction within clouds in (a) CARRIBA measurements (Katzwinkel et al., 2014 fig. 3a therein) and in (b) E2000H simulation around height of 1500m. Similarly, PDF of 90th percentile of vertical velocity is presented for (c) measurements (Katzwinkel et al., 2014 fig. 3c therein) and (d) simulation. The measurements were performed around 100 m below cloud tops, with effective resolution of 20 cm. E2000H simulations results are presented for heights of 1380-1540 m.

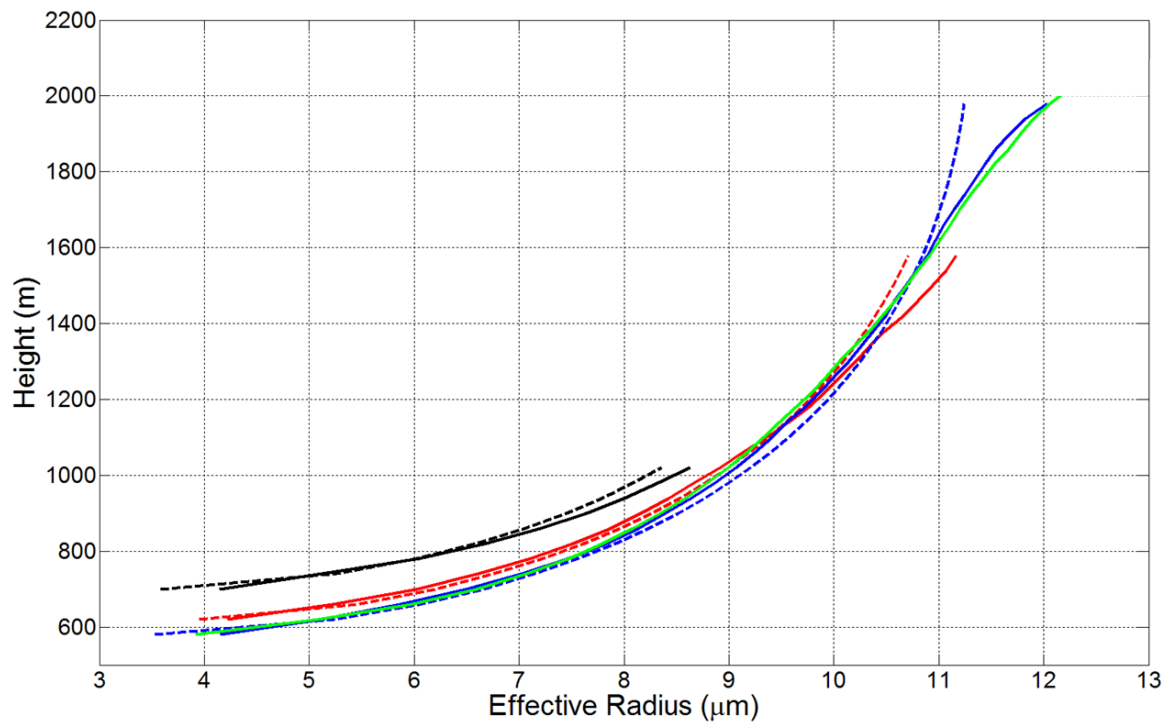


Figure 18. Vertical profiles of averaged simulated (solid lines) and parametrized (dashed lines) effective radii. Blue: E2000H, green: E2000H-50, red: E2000H-RH1, black: E2000H-RH2.